geosciences

MDPI

Article

Seafloor to Borehole CSEM: A 3D Modelling Study of Survey Sensitivity to Small Resistive Targets in Shallow Water

Vikas C. Baranwal [1,2,*], Martin C. Sinha [1], Lucy M. MacGregor [3,4], Anna C. Maxey [1] and Yang Su [5]

[1] National Oceanography Centre Southampton, University of Southampton Waterfront Campus, European Way, Southampton SO14 3ZH, UK; m.sinha@btinternet.com (M.C.S.)
[2] Geological Survey of Norway (NGU), P.O. Box 6315, 7491 Trondheim, Norway
[3] Rock Solid Images, 2600 S Gessner Rd, Suite 650, Houston, TX 77063, USA
[4] Edinburgh Geoscience Advisors Ltd., Azets, Quay 2, 139 Fountainbridge, Edinburgh EH3 9QG, UK
[5] College of Geo-Exploration Sciences and Technology, Jilin University, Changchun 130026, China
* Correspondence: vikas.baranwal@ngu.no

Abstract

Marine controlled source electromagnetic (CSEM) surveys have been proven to be an effective tool in hydrocarbon exploration, principally due to the method's ability (in the right circumstances) to identify electrical resistivity contrasts between hydrocarbon-saturated and brine-saturated sedimentary units. However, the sensitivity of such surveys decreases in shallow water, for deeper targets, and for targets with limited horizontal extent. In principle, the resolution and sensitivity of a survey can be improved by moving either the transmitting or the receiving dipoles into the sub-surface. We have therefore investigated the sensitivity of Seafloor to Borehole CSEM (sbCSEM) survey geometries, specifically for the case of simplified targets with small lateral dimensions in shallow water areas—including targets whose depth of burial substantially exceeds their lateral extent. The results are encouraging. Neither small target size nor shallow water presents obstacles in principle to the use of this approach. Our models reveal distinct lobes in the patterns of electric field and current density amplitudes around a sub-seafloor transmitting dipole. The shape, positions and amplitudes of these lobes are all strongly modified by the presence of one or more small resistive targets, and they are strongly influenced by the positions of target edges. These effects significantly modify the pattern of electric fields at the seafloor and hence result in good sensitivity for realistic survey geometries. Small targets can be detected by seafloor receivers when the sub-seafloor transmitting dipole is located at some distance laterally outside the targets—leading to potential applications in 'step-out' prospecting. The asymmetry of responses at the seafloor from targets that are offset with respect to transmitter location has potential applications in field appraisal, while monitoring of reservoirs during production provides another possible application. Varying the depth of the transmitter down the borehole generates a Vertical EM Profiling (VEMP) survey—analogous to Vertical Seismic Profiling (VSP)—and we demonstrate that this too can have useful applications. Modelling for deeper (3 km sub-seafloor) targets continues to yield encouraging results and suggests that step-out sbCSEM may be effective at depths beyond the detection limit of conventional seafloor–seafloor CSEM.

Keywords: controlled source electromagnetic (CSEM); shallow water; borehole to seafloor; 3-D modelling

Check for updates

Academic Editor: Michela Giustiniani

Received: 20 January 2026
Revised: 21 April 2026
Accepted: 27 April 2026
Published: 29 April 2026

Copyright: © 2026 by the authors. Licensee MDPI, Basel, Switzerland. This article is an open access article distributed under the terms and conditions of the Creative Commons Attribution (CC BY) license.

1. Introduction

In a conventional seafloor–seafloor CSEM survey, a horizontal electric dipole (HED) transmitter is towed near the seafloor and emits low-frequency electromagnetic (EM) signals. After propagating for some distance, these signals are measured using HED receivers at suitable offsets, placed on the seafloor. The modification of amplitudes and phases of these signals as they propagate from transmitting to receiving locations constitutes the CSEM responses of the survey, and these can contain information about the electrical resistivity structure below the seabed. Of particular importance in an economic context, CSEM responses can, in the right circumstances, provide constraints on the presence or otherwise of thin resistive layers associated with hydrocarbon reservoirs [1–3]. Chave and Cox [4] showed that both the source coupling and the sensitivity of CSEM surveys are optimised for this combination (HED-HED) in the presence of a large resistivity contrast across the seabed—as found, for example, over young oceanic crust, where there is little or no sediment cover over the igneous basement. However, in a sedimentary basin, the resistivity contrast across the seabed is much smaller, which tends to improve the coupling of vertical electric dipole (VED) transmitters [5]. VED geometries can also be useful because they are less influenced by the sea surface interaction or 'air wave' effect, which reduces sensitivity to buried resistive structures for HED-HED surveys in shallow water [6–9].

A second motivation for investigating VED geometries is the practical possibility of placing a VED transmitter or receiver within a borehole—for example, an existing well drilled for exploration, appraisal or production purposes. Despite the great advances made by the industry both in geophysical imaging and in geological risk analysis, not all wells achieve their objectives; undoubtedly, many small, undiscovered or unproven panels and reservoirs containing commercially viable hydrocarbon accumulations, close to existing and producing fields, remain unexploited. Our objective is therefore to assess whether and how sbCSEM surveys could add value to existing wells, or to wells in the process of being drilled, or indeed to wells that are deemed unsuccessful owing to their failure to penetrate a hydrocarbon-bearing structure.

Several studies have shown that borehole electromagnetic measurements can be performed successfully, using open-hole wells and fibreglass-cased boreholes, for appraising and monitoring hydrocarbon reservoirs [10]. Tseng et al. [11] have successfully used a borehole-to-surface CSEM survey to locate a saltwater body. Crosshole CSEM surveying has been used for reservoir characterisation and waterflood monitoring by Patzek et al. [12], Wilt and Morea [13] and Colombo and McNeice [14]. Most relevantly, in a marine setting, the general behaviour of the seafloor to borehole CSEM surveying for resistive targets has been investigated by Scholl and Edwards [15], as well as by Maxey et al. [16–18] and by Baranwal and Sinha [19,20]. In the last decade, there have been more developments in simulating the VED sources in the steel-cased boreholes for CSEM modelling and inversion [21,22].

Boreholes are cased as well, generally using steel, which is highly conductive. There have been several studies to model the steel casing effects and include the steel casing in the forward modelling and inversion [21–27]. Steel casing is often considered a hindrance, but it helps transmit low-frequency signals deep into the formation, allowing it to act as a conductive source/antenna that enhances the detection of surrounding resistivity contrasts. It distorts electromagnetic fields as well. The casing effect dominates at close distances (200–300 m from the well), but for far-enough distances (>500 m) and for transmitters placed far below the casing shoe, the formation response can still be detected well and unaltered.

In this paper, we present the results of a numerical modelling study of an sbCSEM setup, which uses a VED transmitter located in a borehole and receiver responses mea-

sured at the seafloor. We have not considered the steel casing effects to keep our forward modelling study simple and directly relatable to fibreglass-cased or open-hole wells.

Since the principles of reciprocity of transmitting and receiving dipoles apply [28–30], our results could equally be used for the case of a mobile transmitting dipole at the seafloor and a VED receiver in the borehole. The single VED source configuration is most computationally efficient for this modelling study, and would in practice allow the collection of survey data from many water column receivers simultaneously, minimising the well time required for a survey. However, the logistical, engineering and safety challenges of operating a powerful electric dipole transmitter in a borehole are formidable. In engineering terms, the use of VED receivers within the borehole and one or more mobile transmitting dipoles within the water column would be more straightforward, but possibly at the cost of requiring more well time to complete a survey.

We have chosen to concentrate on a specific set of circumstances, all corresponding to a 'difficult' or 'challenging' target for conventional marine CSEM surveys. These include shallow water, representative of shallow shelf seas on the upper parts of continental margins or in intracontinental basins; laterally small targets, with horizontal dimensions comparable to or less than their depth of burial; and, in the later sections, relatively deep targets (2 to 3 km sub-seafloor). The results of our study may be particularly relevant to mature oil provinces such as the North Sea, where substantial production infrastructure is already in place; where numerous wells have been drilled; and where small, unproven and therefore undeveloped reservoirs or panels may exist close to existing wells.

As well as modelling the most favourable situation, in which a VED can be placed in a borehole that penetrates the resistive reservoir target, we have also modelled situations in which the borehole misses the target completely, or in which the maximum depth of the borehole is less than that of the target. We also investigate situations with two offset target structures close to one another, for cases in which the borehole penetrates one but not both, and for cases in which the borehole fails to penetrate either target. Possible future applications of sbCSEM based on this approach may include step-out exploration from existing wells; 'downward looking' sbCSEM, to refine knowledge of structures ahead of the well; and vertical CSEM profiling (VEMP).

Lastly, there is a need to improve our ability to use geophysical methods to monitor and, especially, to quantify for audit and verification purposes, as well as the emplacement and migration of carbon dioxide which has been captured and injected into reservoirs for the purpose of long-term geological storage ('sequestration'). This can include situations in which it is undesirable for a well to pierce the cap rock above a reservoir (an example might be the Sleipner CO_2 storage project [31]), and in these cases, transmitting or receiving dipoles placed in the subsurface but above the reservoir seal may produce higher resolution results than those available from seafloor to seafloor surveys.

2. Earth Resistivity Models

Our objective is to assess whether seafloor to borehole CSEM surveying can be applied usefully in a particular set of geological and economic circumstances. We have therefore chosen to model specific resistivity structures and survey layouts which, although geometrically simplistic, are relevant to this context. Figure 1a schematically shows both the basic layout of our modelled survey and the background resistivity structure. A layer of seawater, 100 m thick and with resistivity of 0.3 Ω·m, overlies the solid earth, which, for this case, consists of a uniform half-space of resistivity of 1 Ω·m. This constitutes our *half-space reference model*. The transmitter consists of a 25 m long vertical electric dipole (VED), which we assume to be placed beneath the seafloor, within a borehole. A number of receivers are placed immediately above the seafloor, so that their sensors are within

the water column, at a range of horizontal offsets from the transmitter location. We have modelled both horizontal and vertical components of the electric field at the receivers. The transmitter is located at the origin in the x-y plane, and the receivers are placed along y = 0. Resistive target structures are located symmetrically about y = 0, and the horizontal component of the electric field modelled at the receivers is usually the x-component (which, for this case, is also the radial component).

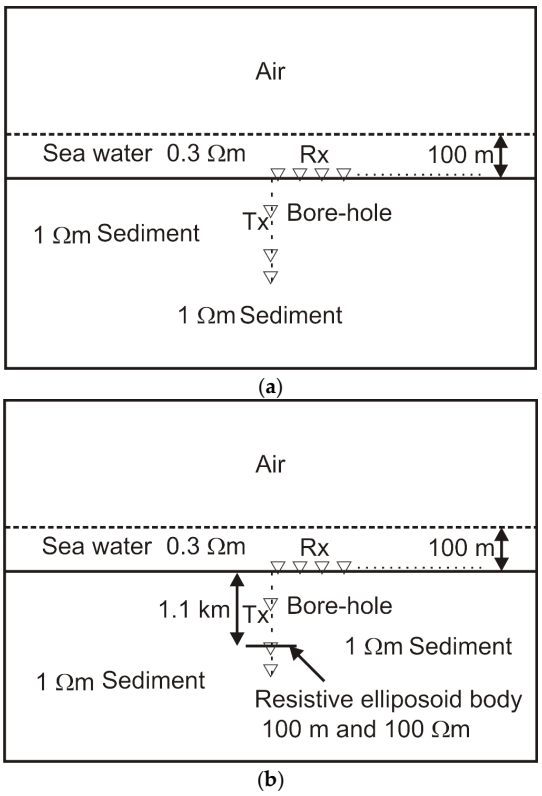


Figure 1. Schematic diagram of the resistivity structure and survey layout for (**a**) our *half-space reference model* and (**b**) our *centred resistive disk model* (not to scale). Dashed line symbolises water surface and triangles symbolise transmitter (Tx) and receivers (Rx).

The basic target which we have modelled consists of a resistive disk, is 100 m thick, and is buried 1.1 km beneath the seafloor (Figure 1b). The disk has a resistivity of 100 Ω·m and a radius of 712.5 m (diameter of 1425 m). In the *centred resistive disk model*, the VED transmitter is located within and at the centre of the target disk. In the Section 5.1, we have also modelled a number of scenarios in which the target disk is displaced laterally, along the x-axis, with respect to the transmitter. Two particular cases are the *just inside model*, in which the transmitter is located 12.5 m inside the perimeter of the resistive target, and the *just outside model*, in which the transmitter is located 12.5 m beyond the perimeter of the target.

In addition to the small resistive disk target, we have also modelled (purely for comparison) the 1D case (resistivity varies only along the z-axis) of a layer that extends infinitely in the x and y directions, with the same resistivity, depth of burial and thickness as the target in the *centred resistive disk model.* We refer to this as the *thin resistive layer model*.

In the Section 5.4, we also investigate a *stacked reservoir model*. Here, a second resistive disk target with the same dimensions and properties as the *centred resistive disk model* is added to the structure, at a depth 200 m deeper than the first target. The second deeper resistive target is offset laterally from the first target, with its centre located 1400 m along the positive x-direction from that of the standard target. It has the same dimensions and

resistivity as the first target, so the edges of the two resistive features just overlap in the x-direction. In the Section 5.5, we investigate a number of scenarios in which the depth of the target resistive body or bodies is increased to 2 or 3 km. Table 1 represents a summary of the standard model parameters used in the present study.

Table 1. Description of parameters for various standard models used for modelling in the present work. All the models have the following parameters in common: transmitter—25 m long VED and centred at (0, 0, −1250), half-space resistivity—1 Ω·m, sea water resistivity—0.3 Ω·m, sea water thickness—100 m, disk thickness—100 m, disk resistivity—100 Ω·m, and disk diameter—1425 m (Figure 1). The *thin resistive layer model* consists of an infinite layer in the x and y directions with a thickness of 100 m and a resistivity of 100 Ω·m.

Model	Centre of Disk-1			Centre of Disk-2			Centre of Layer		
	X (m)	Y (m)	Z (m)	X (m)	Y (m)	Z (m)	X (m)	Y (m)	Z (m)
Half-space reference	-	-	-	-	-	-	-	-	-
Thin resistive layer	-	-	-	-	-	-	0	0	−1250
Centred resistive disk	0	0	−1250	-	-	-	-	-	-
Just inside	700	0	−1250	-	-	-	-	-	-
Just outside	725	0	−1250	-	-	-	-	-	-
Stacked reservoir	0	0	−1250	1400	0	−1450	-	-	-

In all of these models, the low resistivity background material represents water saturated marine sediments. The resistive disk structures correspond to targets of economic interest. In the case of hydrocarbon exploration, the targets would correspond to small oil or gas reservoirs, or undeveloped pockets, close to existing exploration or appraisal wells or to existing production systems. Alternatively, they may correspond to known accumulations of oil or gas, with the survey being undertaken either for field appraisal prior to development, or for reservoir monitoring during production. Thirdly, the resistive disk targets can be taken to represent reservoirs used for long-term geological storage (sequestering) of CO_2—in which case the relevance of our modelling is to monitor and verify such schemes, including quantitative assessment of rates and directions of lateral migration of CO_2 from its injection point.

A limitation of our models is that we have placed our transmitting dipole directly within the geological structure, without taking into account either the resistivity structure of the borehole itself or any casing that might be present. The issue of well casing and its effect on geophysical results is complex [22,32]. The electromagnetic effects of the well itself will depend on whether it remains filled with oil-based or water-based mud, or indeed whether it is being used for hydrocarbon production or for injection purposes. The detailed modelling of the effects of the well and its casing would therefore have to be undertaken on a case-by-case basis and is outside the scope of this study. However, it is common for many wells, even after completion, to have an uncased section—sometimes some hundreds of metres in length—at the bottom. It is also normal practice during the drilling of exploration and appraisal wells to leave lower sections uncased for at least as long as it is needed for wireline logging to be completed. Some uncased well sections are therefore likely to be available for sbCSEM studies.

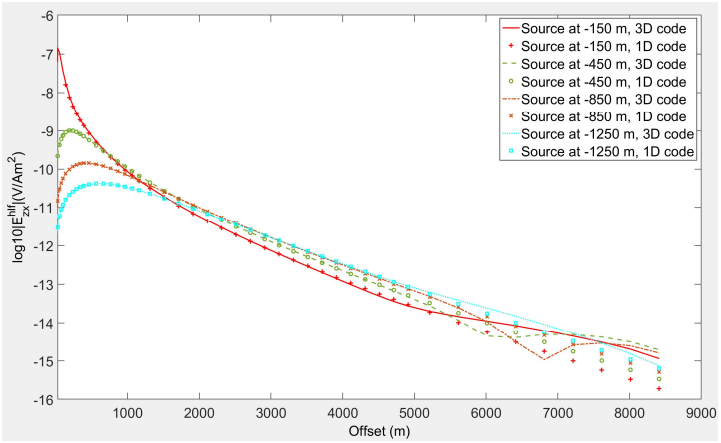
3. Numerical Modelling Method

We carried out the numerical modelling using the EH3D code [33] developed at the Geophysical Inversion Facility, University of British Columbia. The EH3D code is based

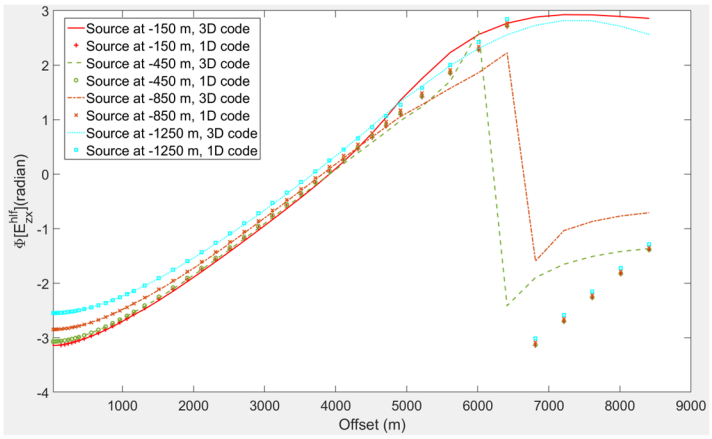
on finite volumes using a staggered grid and enables us to calculate all the components of electric and magnetic fields at each grid node. In this study, we focus on electric fields only.

The first stage of our modelling was to verify the stability and resolution of our grid by comparing the predictions of the 3D code against those for an identical Earth model from a 1D code. For this, we used versions of the HED 1D code of Chave and Cox [4], extended and modified (Andreis and MacGregor [9] to allow computations for VED sources and receivers. In all cases, the verification comparisons used a VED transmitter. The first comparison is for the x- or radial component of the horizontal electric field at the receiver. We refer to this as E_{zx}, where the first subscript denotes the orientation of the transmitter, and the second the orientation of the receiver. The second comparison is for the vertical electric field at the receiver, denoted by E_{zz}.

Figures 2 and 3 show plots of amplitude and phase of E_{zx} and E_{zz} respectively for VED transmitters located at depths of 150 m, 450 m, 850 m and 1250 m below sea surface, computed using the EH3D and 1D codes. For each source depth, lines represent the EH3D result and symbols represent the 1-D code result. There is good agreement between the two codes, at least up to horizontal offsets of 5 km for E_{zx} and 6 km for E_{zz}. Beyond these offsets, edge effects from the boundaries of the 3D mesh begin to produce distortions. We conclude that our modelling procedure and mesh structure are valid for horizontal offsets up to 5 km.



(**a**)



(**b**)

Figure 2. Comparison of (**a**) amplitude normalised to unit source dipole moment and (**b**) phase of horizontal component of the electric field at the seafloor as a function of horizontal source–receiver offset, as calculated for the *half-space reference model* and for varying source depths by the EH3D and 1D codes.

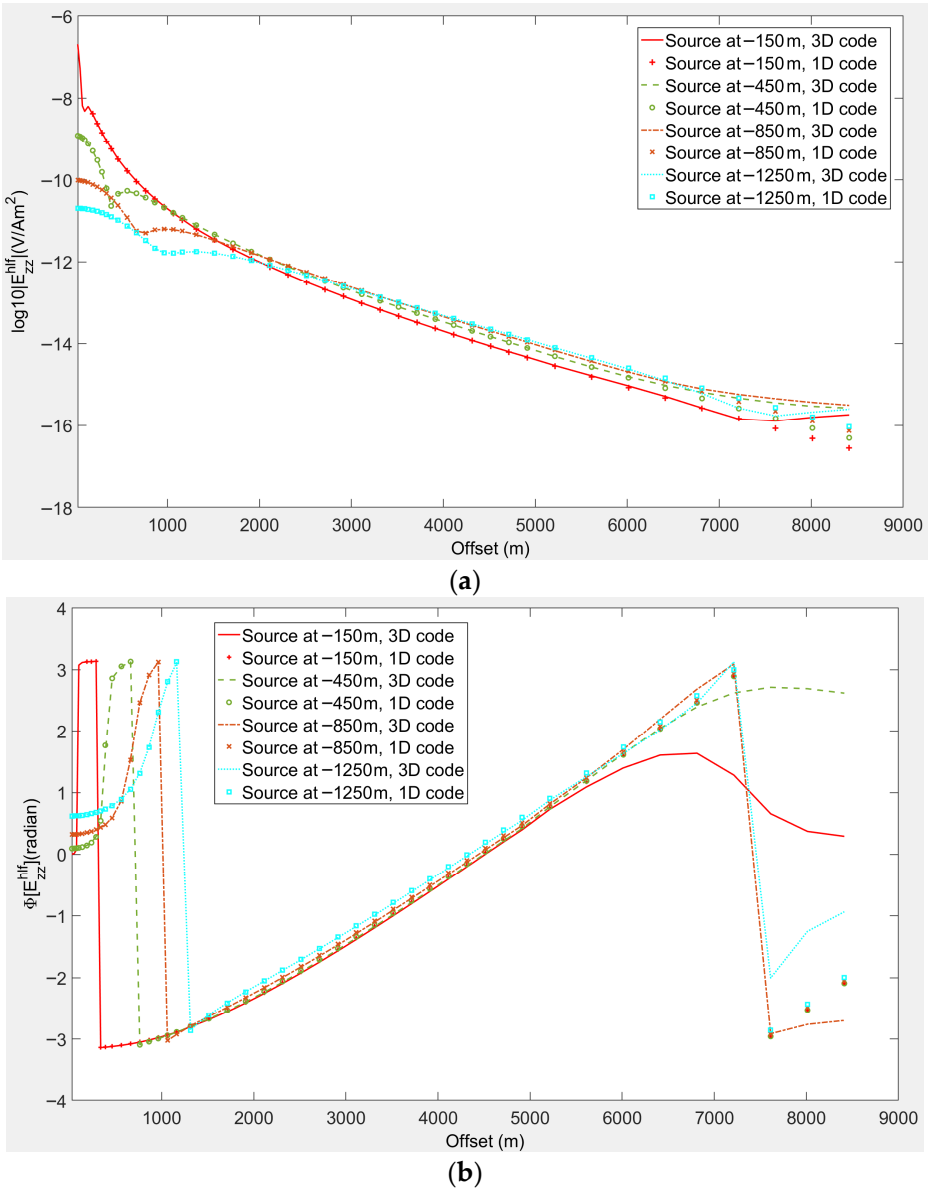


Figure 3. Comparison of (**a**) amplitude normalised to unit source dipole moment and (**b**) phase of vertical component of the electric field at the seafloor as a function of horizontal source–receiver offset, as calculated for the *half-space reference model* and for varying source depths by the EH3D and 1D codes.

The second task was to select an appropriate frequency for the remainder of the study. A frequency range of 0.1 to 10 Hz is commonly used for marine CSEM modelling [23,26,27]. Therefore, a 3D modelling was performed for various frequencies ranging from 0.03 Hz to 3.16 Hz for the *centred resistive disk model*. An optimum frequency for any survey will ideally combine observable inflexion points in the fields at the seafloor associated with the edges of the target (seen best at high frequencies) with receiver amplitudes that are sufficiently large to be detectable (seen best at low frequencies). The logarithmic amplitude of the horizontal and vertical electric fields calculated at the seafloor for the various frequencies is plotted in Figure 4. A frequency of 0.31 Hz represents an optimum trade-off for this case between curvature and amplitude of the responses; therefore, this frequency was used for all further modelling.

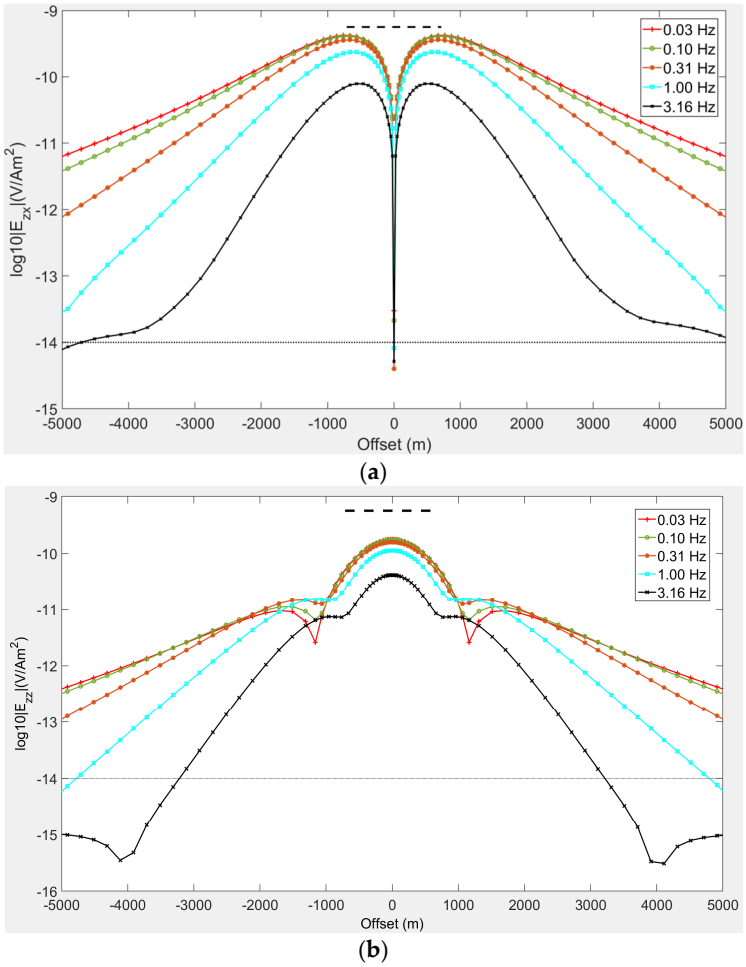
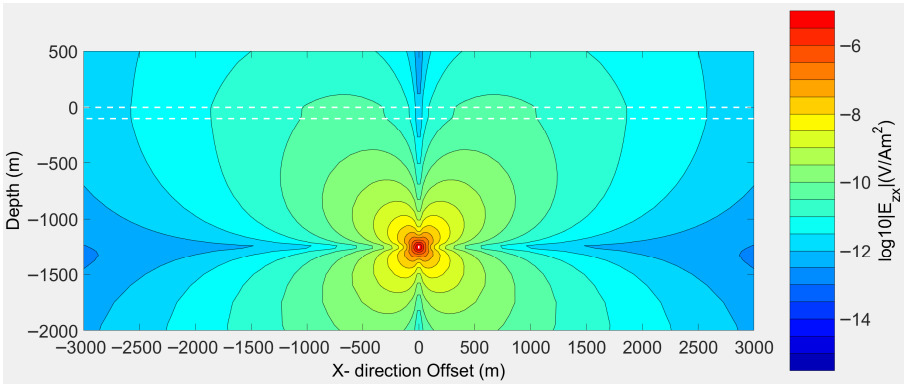


Figure 4. The variation in electric field amplitudes normalised to unit source dipole moment for (**a**) horizontal and (**b**) vertical components of the electric field as a function of horizontal offset, calculated at the seafloor for the *centred resistive disk model* at a range of frequencies. The transmitter is a 25 m long VED with 0 offset and at a depth of 1.1 km below the seafloor. The water depth is 100 m. The location of the disk is plotted with black dashed lines.

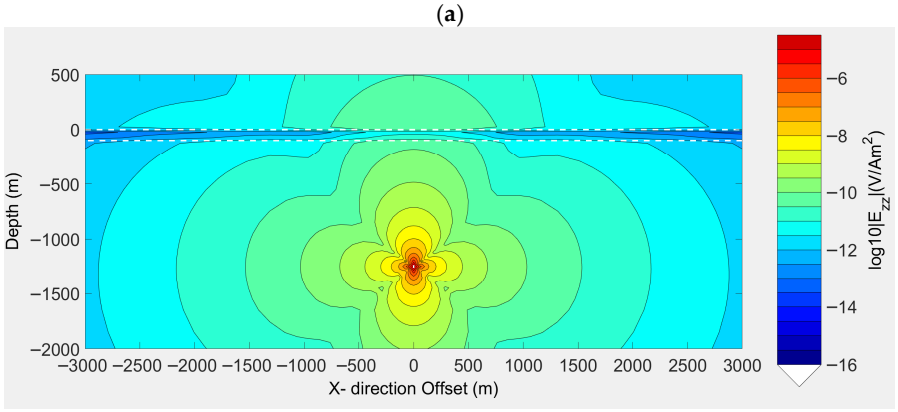
4. Dimensionless Amplitudes and Patterns of Induction

In this section, we present plots of the x- and z-components of electric field amplitudes, in the xz plane at y = 0, for the *half-space reference model* and the *centred resistive disk model*. The y-component of the electric field amplitude is zero everywhere in this plane, due to symmetry, for all of our models. As mentioned above, we refer to the two components as E_{zx} and E_{zz} respectively, where the first subscript corresponds to the transmitter orientation (z for VED) and the second subscript corresponds to the component at the receiver.

Figure 5 shows amplitude normalised to unit source dipole moment of the x- and z-components of the electric field for the *half-space reference model*. Due to both inductive losses and the $1/r^3$ amplitude behaviour of any dipole field, amplitudes decrease very rapidly away from the transmitter, with a factor of about 10^{12} difference in amplitude between the centre and the edges of each plot. Also, clearly visible are the expected lobate amplitude patterns, with maxima along the directions at 45° and 135° from the vertical, and minima along the horizontal and vertical directions on the E_{zx} plot, and vice versa on the E_{zz} plot. It can also be seen that the vertical field amplitudes are substantially smaller in the water column and larger in the atmosphere than in the subsurface. This is largely due to the galvanic response to the resistivity contrasts across the seafloor and sea surface, as discussed below.



(**a**)



(**b**)

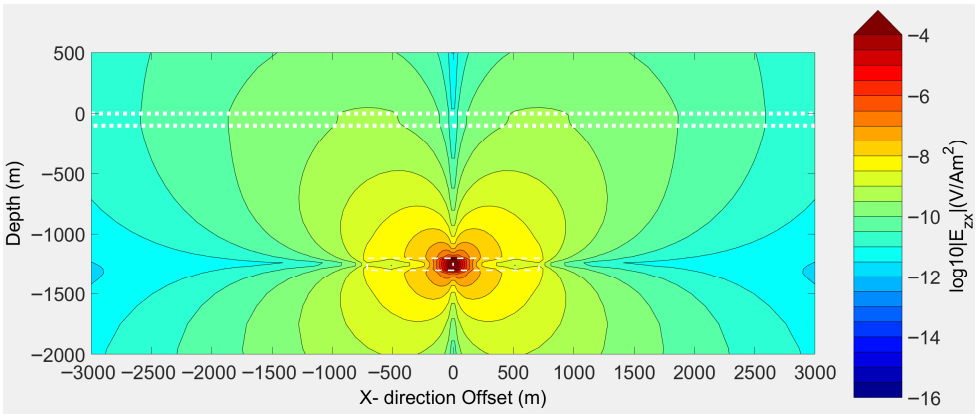
Figure 5. Amplitude normalised to unit source dipole moment of (**a**) the horizontal and (**b**) the vertical components of the electric field in the xz plane through the transmitter, for the *half-space reference model*. Water layer is shown by white dotted lines. Transmitter is shown by a white marker.

Figure 6 shows the equivalent plots for the *centred resistive disk model*. Several differences are immediately apparent. Firstly, amplitudes are larger everywhere. This is partly because inductive losses immediately around the transmitter are less, since it is in a more resistive part of the model. However, a large part of the difference is simply that the dipole moment is unchanged between Figures 5 and 6, and so, the current emitted from the two ends of the dipole is the same. Since, in Figure 6, the dipole is in a local medium that is 100 times more resistive, a much larger potential difference would be required to drive the transmitter current in this case. Electric field amplitudes are larger everywhere in Figure 6 than in Figure 5, principally because, in the case of Figure 6, a much larger voltage (and hence power) would need to be applied to the transmitting dipole to maintain its dipole moment.

A second difference between the two plots is that, in the *centred resistive disk model*, the horizontal electric fields inside the target body are smaller than those outside it, while the vertical electric fields are larger inside it than outside it.

The steep gradient in electric field amplitudes away from the transmitting dipole (i.e., over about 10^{12} orders of magnitude) in both Figures 5 and 6 tends to mask much of the more interesting aspects of the behaviour of the fields within the model, even when amplitudes are plotted on a logarithmic scale as here. We have therefore plotted dimensionless amplitudes of both the horizontal and vertical components of the electric field [34] in subsequent figures. Dimensionless amplitudes have the advantage that they compensate for the $1/r^3$ decrease in amplitude away from a dipole source—in effect, a 'geometric spreading' correction. Secondly, they take into account variations in local resistivity at either hypothetical or real receiver locations, so that they correspond to variations in the amplitude of the current density rather than the electric field. In the low

frequency limit, current density normal to a boundary between two regions of contrasting resistivity is continuous, whereas electric field along the same direction is discontinuous, and varies in inverse proportion to the resistivity contrast. This makes the dimensionless amplitude less sensitive than conventional electric field amplitude to purely galvanic behaviours (i.e., those that occur even in the DC case), and hence relatively more sensitive to the inductive behaviour.



(**a**)

(**b**)

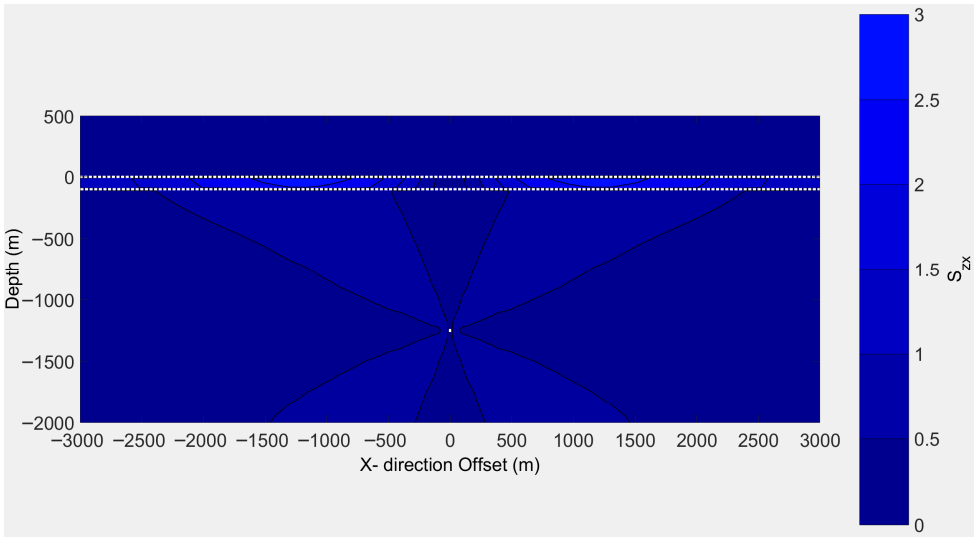
Figure 6. Amplitude normalised to unit source dipole moment of (**a**) the horizontal and (**b**) the vertical components of the electric field in the xz plane through the transmitter, for the *centred resistive disk model*. Water layer is shown by white dotted lines. Locations of the transmitter and resistive disk are marked by a white marker and white dashed lines, respectively.

Dimensionless amplitude is expressed as:

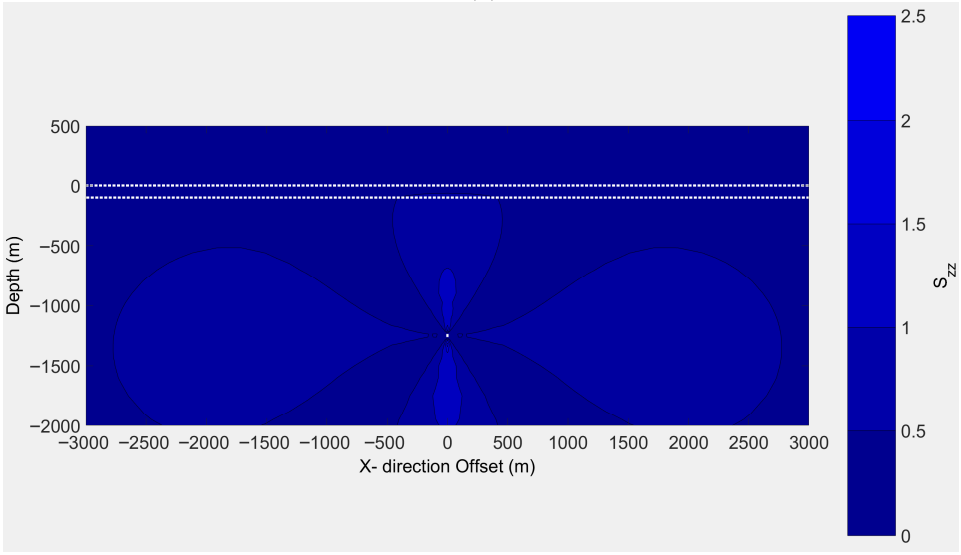
$$S_{zx} = \frac{2\pi E_{zx} r_s^3}{\rho_r M}, \text{ and } S_{zz} = \frac{2\pi E_{zz} r_s^3}{\rho_r M} \quad (1)$$

where S is the dimensionless amplitude, E is the electric field amplitude (units Vm^{-1}), M is the transmitter dipole moment (units Am), r_s is the slant range (in m) between the transmitter and the receiver and ρ_r is the local resistivity at the receiver. The amplitude normalised to unit dipole, with units $\mathrm{VA}^{-1}\mathrm{m}^{-2}$, is equal to E/M.

Figures 7–9 show the patterns of S_{zx} and S_{zz} for the *half-space reference model*, the *thin resistive layer model* and the *centred resistive disk model* respectively. Note that in these and subsequent figures, S is presented on a linear, not logarithmic, scale. Note that for ease of comparison, the colour scale is the same in all three pictures.



(**a**)



(**b**)

Figure 7. Dimensionless amplitudes of (**a**) the horizontal and (**b**) the vertical components of the electric field in the xz plane through the transmitter, for the *half-space reference model*. Water layer is shown by white dotted lines. Transmitter is shown by a white marker.

The pronounced differences in the behaviour of the fields for the three contrasting models are clearly seen in these plots. In Figure 7, the lobate patterns for the two components described above can clearly be seen. We also note from Figure 7 that vertical current densities in the water column are very small, while horizontal current densities in the water layer are large above the upper lobes. The combination of current channelling within the conductive water layer and current blocking by the extremely resistive atmosphere is forcing current to flow predominantly horizontally in the water layer at these locations.

In Figure 8, we note that the thin resistive layer strongly modifies the field patterns. Horizontal current densities are increased in the water layer at medium and long offsets and are also increased in the background sediment material immediately above and below the resistive layer. Horizontal current densities are small within the resistive layer at long offsets as well (Figure 8a). In contrast, vertical current densities are greatly increased within, above and below the resistive layer at long offsets (Figure 8b).

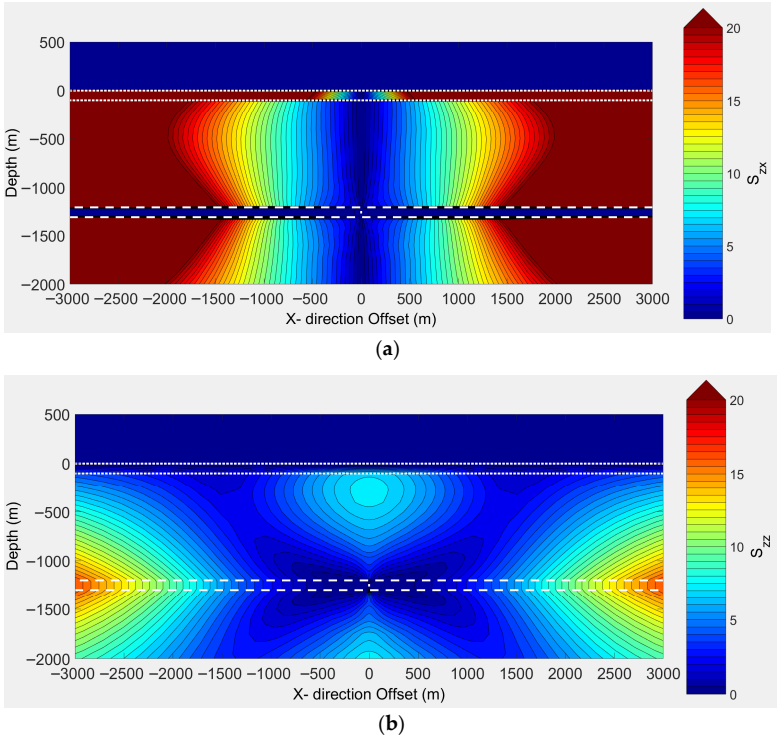


Figure 8. Dimensionless amplitudes of (**a**) the horizontal and (**b**) the vertical components of the electric field in the xz plane through the transmitter, for the *thin resistive layer model*. The locations of the disk and source are also plotted. Water layer is shown by white dotted lines. Locations of the transmitter and thin resistive layer are marked by a white marker and white dashed lines, respectively.

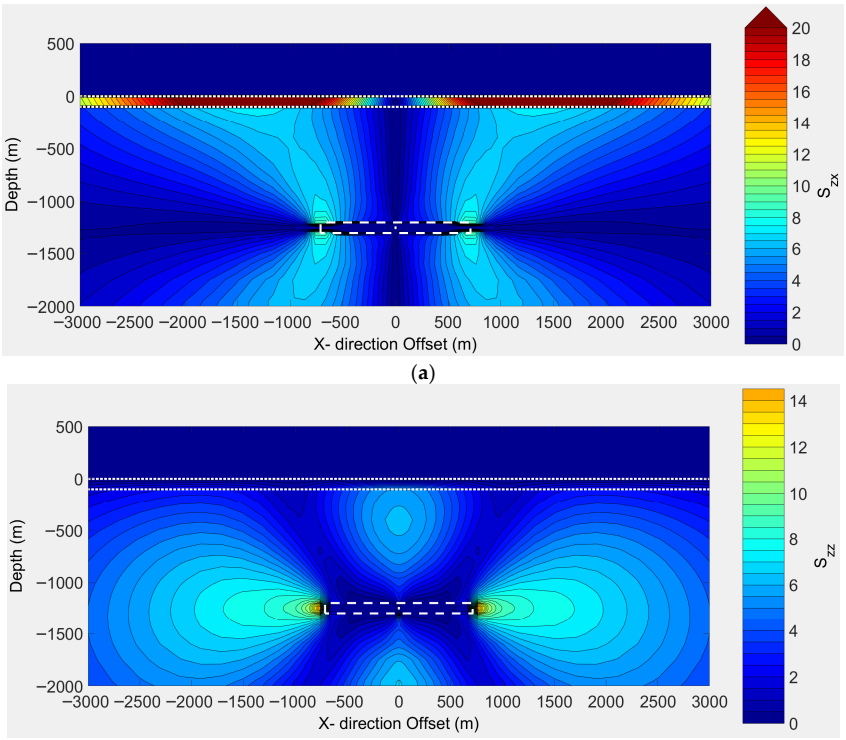


Figure 9. Dimensionless amplitudes of (**a**) the horizontal and (**b**) the vertical components of the electric field in the xz plane through the transmitter, for the *centred resistive disk model*. Water layer is shown by white dotted lines. Locations of the transmitter and resistive disk are marked by a white marker and white dashed lines, respectively.

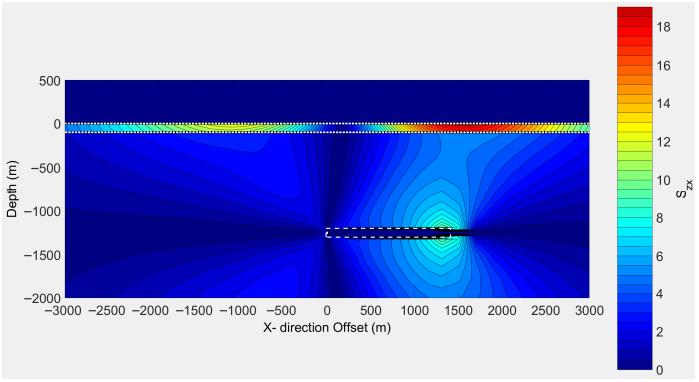
In the *centred resistive disk model* (Figure 9), the patterns of S_{zx} and S_{zz} both clearly respond to the locations of the edges of the resistive target. In Figure 9a, the maxima lobes are moved outwards, while the current density in the overlying water column is again at its greatest above the upper lobes. This suggests that the S_{zx} component should show good sensitivity to the spatial extent of the target body. In Figure 9b, the periphery of the resistive target appears to be behaving as an annular emitter of vertical current density. This suggests that the S_{zz} component should also have good sensitivity to the lateral extent of the target.

We can clearly see from Figures 7–9 that dimensionless amplitude components present a better insight into the interactions between the source and the resistivity structure. We note the following advantages of using dimensionless amplitudes. Firstly, it applies a correction for the huge variations in amplitude caused by geometric spreading, so that the patterns we observe are no longer dominated by this effect. Secondly, the values of the dimensionless amplitudes no longer vary through many orders of magnitude. We can use linear rather than logarithmic amplitude plots. Finally, the patterns observed are more closely related to inductive behaviour and the presence of secondary fields, rather than the geometrical decrease in the primary fields. Therefore, we will present plots of dimensionless amplitude only for further models.

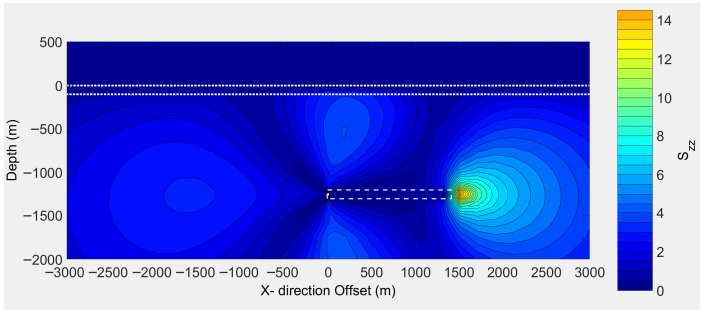
5. Modelling Results

5.1. Offset Targets

Figures 10 and 11 show the patterns of dimensionless amplitudes for the *just inside model* and the *just outside model*. We can clearly observe asymmetry in the amplitudes in both plots, reflecting the offset target position; note that this asymmetry is observable for both components at the seafloor, as well as in the subsurface—a positive result for a practically realisable survey.



(**a**)



(**b**)

Figure 10. Dimensionless amplitudes of (**a**) the horizontal and (**b**) the vertical components of the electric field in the xz plane through the transmitter, for the *just inside model*. Water layer is shown by white dotted lines. Locations of the transmitter and resistive disk are marked by a white marker and white dashed lines, respectively.

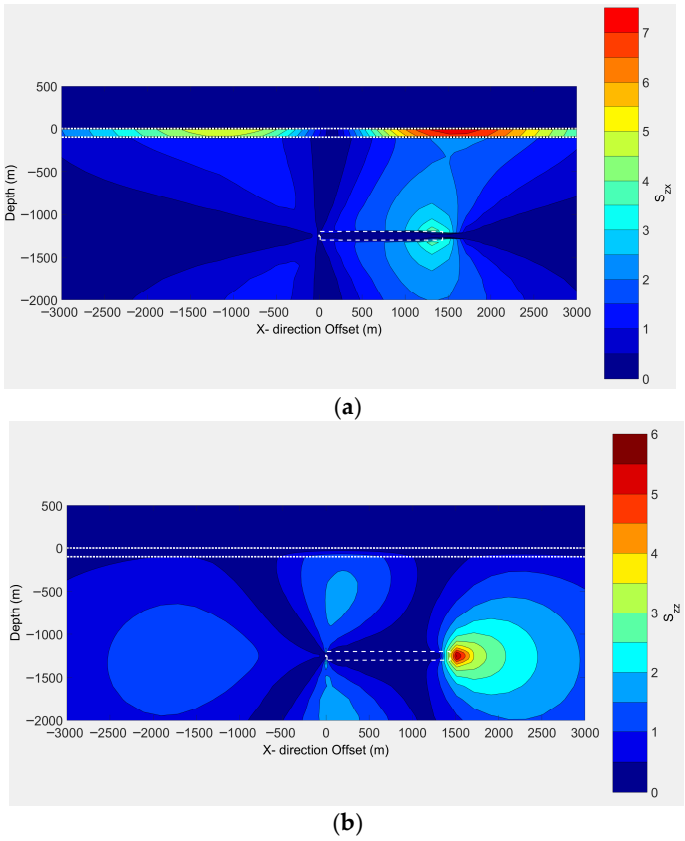


Figure 11. Dimensionless amplitudes of (**a**) the horizontal and (**b**) the vertical components of the electric field in the xz plane through the transmitter, for the *just outside model*. Water layer is shown by white dotted lines. Location of the transmitter and resistive disk are marked by a white marker and white dashed lines, respectively.

An important distinction between the two cases is that while in Figure 10 the transmitter is still inside the resistive target, in Figure 11, the transmitter is outside the target. The galvanic consequences of this, as discussed above (i.e., the decrease in voltage and power required to drive the source current from the transmitter in the more conductive background sediments), are chiefly responsible for the generally lower amplitudes observed in Figure 11 than in Figure 10 (note the differences in scale bars). However, in Figure 11, we continue to see marked asymmetry in both sets of responses. In particular, the far perimeter of the target body again appears to be acting as an induced emitter of fields for both components. This has important practical implications for exploration, appraisal and monitoring—a well that 'misses' a target laterally can still be valuable for sbCSEM survey purposes, in both detecting a resistive target and delineating its lateral boundaries.

While these plots usefully illustrate the pattern of induction that occurs in the subsurface, any practical application of sbCSEM depends upon measurements made in the water column. Therefore, we have extracted the responses at the set of node points 12.5 m above the seafloor for the remainder of this section.

5.2. Seafloor Responses for the Standard Models

The S_{zx} and S_{zz} responses just above the seafloor are plotted for the various models in Figure 12, along a linear profile parallel to the x-axis and passing above the centre of the target and the transmitter location. The *centred resistive disk* and *half-space reference* model responses are symmetrical on both sides of the transmitter as expected, due to the symmetry of the models. The magnitude of the responses and the lateral positions of

maxima and minima in the responses are influenced both by the depth of the VED dipole source (although this is not illustrated here) and also by the edges of the resistive body.

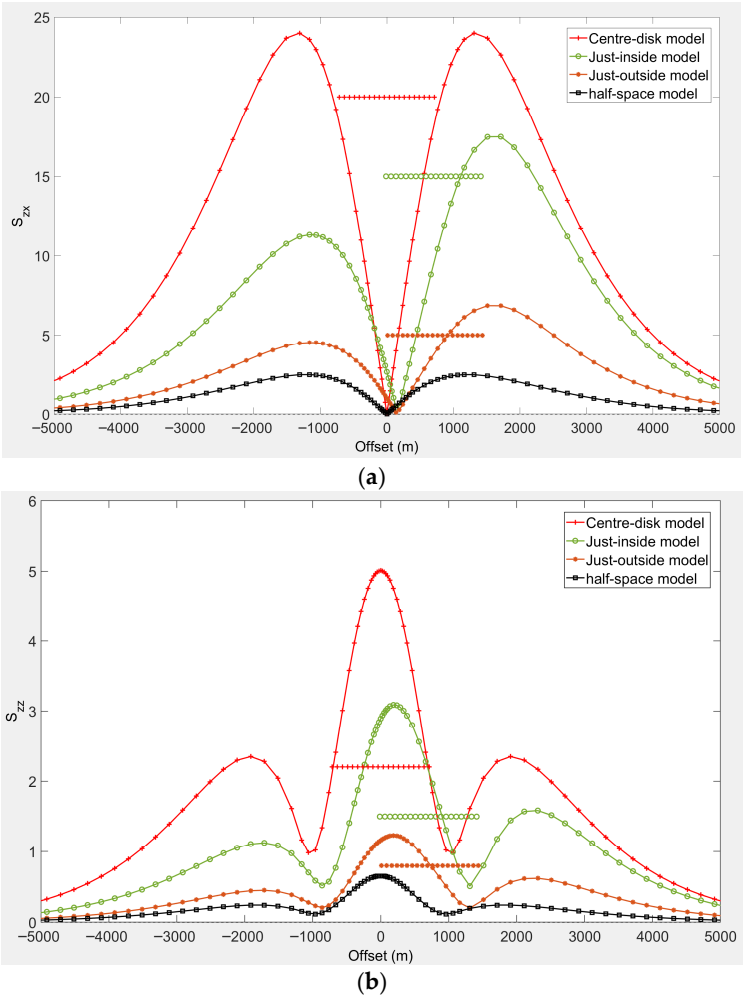


Figure 12. Dimensionless amplitudes of (**a**) the horizontal and (**b**) the vertical components of the electric field at the seafloor for various models. The locations of the disk are also plotted with corresponding colour markers, and they only vary in the horizontal direction, not in the vertical direction.

The responses for the *just inside* and *just outside* models are asymmetric along the profile. The minimum (in the case of S_{zx}) and maximum (in the case of S_{zz}), which are observed directly above the source position (x = y = 0) for the symmetric models, are shifted laterally for the non-symmetric models, reflecting the change in the position of the edges of the resistive body. Similarly, the locations of the local maxima in S_{zx} and minima in S_{zz} at between 0 and 2 km offsets are shifted laterally by appreciable distances in the non-symmetric model responses. This behaviour would clearly be useful in reservoir monitoring and appraisal applications.

To illustrate how the responses vary laterally at the seafloor in both the x and y directions, Figure 13 shows two plan views for the *just outside model*. For values of y not equal to 0, it is useful to resolve the horizontal component into radial and tangential components—so the two panels show $S_{z,rad}$ and $S_{z,tan}$ components respectively. Panel (a) illustrates very clearly the asymmetric pattern of the response, corresponding to the offset location of the resistive target with respect to the transmitting VED. Panel (b) shows something rather different. In a 1-dimensional or radially symmetric (about a VED transmitter) resistive structure, the tangential horizontal component of the electric field would be zero

everywhere. Panel (b), therefore, corresponds to a 'null-coupled' component of the field. In this case, where the resistivity structure is neither 1-D nor radially symmetric, the non-zero values of the tangential component are therefore highlighting the edge of the resistive body where it is closest to the transmitter. This use of the null-coupled tangential component could provide an additional valuable application of sbCSEM for delineating the boundaries of anomalously resistive bodies.

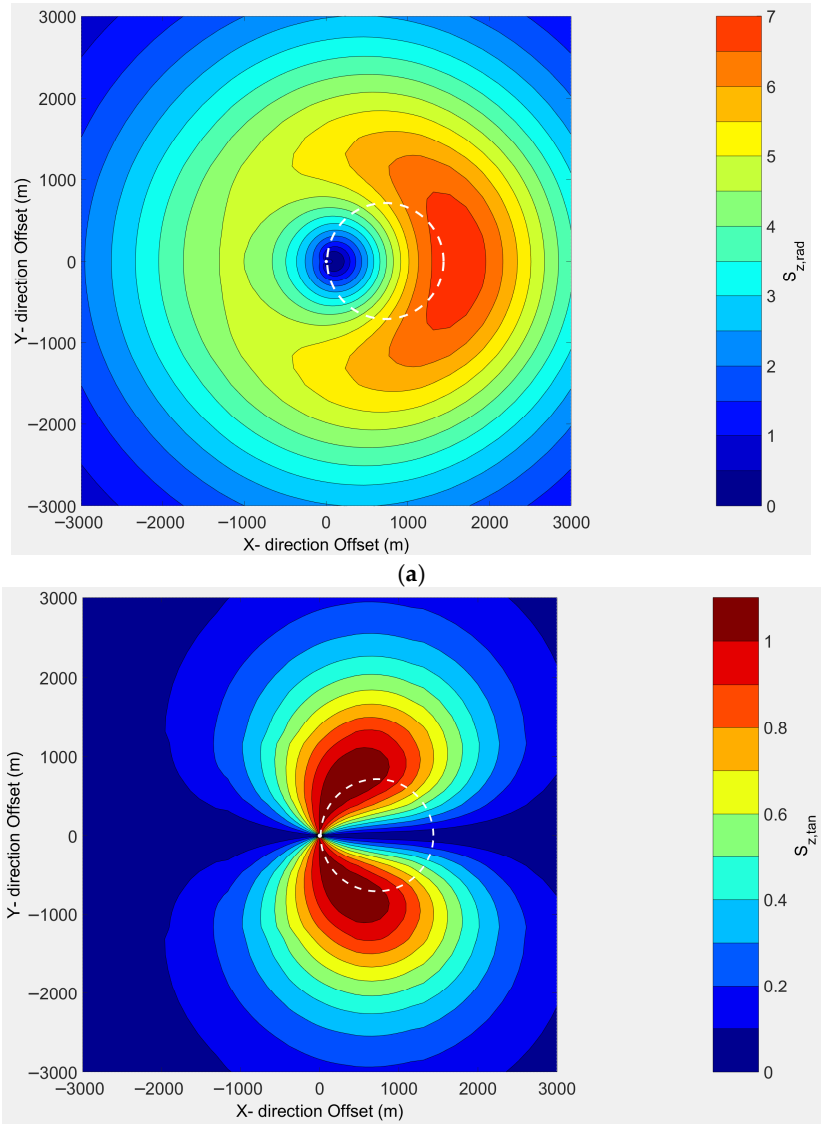


Figure 13. Contour plot of a plan view of horizontal dimensionless amplitude response at the seafloor for the *just outside model*. (**a**) $S_{z,rad}$ component. (**b**) The null-coupled $S_{z,tan}$ component. The locations of the disk and source are also plotted. Locations of the transmitter and resistive disk are marked by a white marker and white dashed lines, respectively.

5.3. Maximum Detectable Offset of the Target from the Transmitter

After investigating these responses for the *just inside* and *just outside* models, we moved the small resistive target progressively further away from the transmitter location, while keeping its dimensions and other properties constant. This simulates a case where the transmitter is placed in a well which has missed the resistive target laterally by up to several hundred metres. We modelled three new offset positions, in which the distance from the nearest point on the perimeter of the small resistive body to the borehole increased to 400 m, 700 m and 1000 m. The VED transmitter of 25 m length was placed at the centre

of the mesh and at 1150 m depth below the seafloor as before. The horizontal and vertical components of the dimensionless amplitude of the electric field at the seafloor are plotted in Figure 14. In all cases, the amplitudes and lateral locations of local maxima and minima in the responses are significantly affected by the presence of the resistive body. The minimum detectable electric field amplitude in marine CSEM is reported as 10^{-14}–10^{-15} V/Am^2 with 5–10% of uncertainty [35,36]. Therefore, we assumed a noise floor of 10^{-14} V/Am^2. The noise floor (equivalent to 10^{-14} V/Am^2 in electric fields) is shown by dashed lines in Figure 14, which coincides with the 0 level on the y-axis. The location of the source dipole at various offsets and the location of the disk with its lateral extent are also plotted.

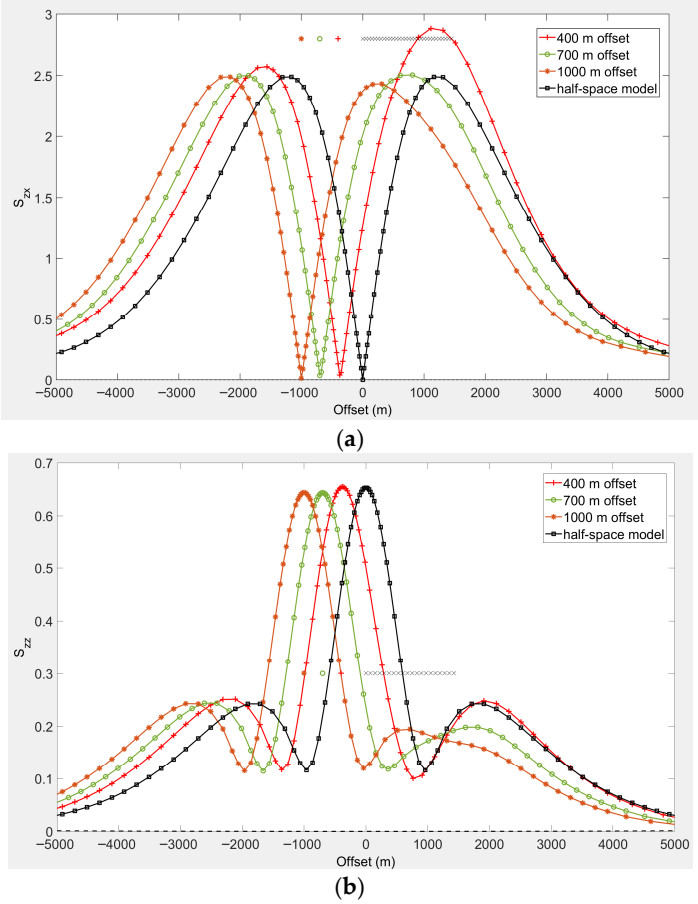


Figure 14. Dimensionless amplitudes of (**a**) the horizontal and (**b**) the vertical components of the electric field at the seafloor for variants of the *resistive disk model* with a range of horizontal offsets of the borehole from the nearest edge of the target. The locations of the offset source are plotted with corresponding colour markers, and the resistive target is plotted by black 'x' markers.

Figure 15 shows a plot of percentage differences in horizontal and vertical components of the dimensionless amplitude of the electric field at the seafloor, relative to the corresponding *half-space reference model* response. We have assumed a noise floor of 10^{-14} V/Am^2. Note that the percentage difference in dimensionless amplitudes and the percentage difference in electric field are essentially the same because of cancelling out the common parameters when taking a ratio with respect to the half-space or any other model. Again, this shows that the standard resistive disk placed at various offset locations is detectable from the modelled field components. A 5% uncertainty level for S_{zx} and S_{zz} will be 5 in amplitude for the percentage difference in S_{zx} and S_{zz} in Figure 15. The response is well within detectable limits for these models. It is more readily distinguished in the vertical components than in the horizontal components, but the magnitude of the vertical component is smaller. The amplitude of the vertical electrical field for the *half-space reference model* at around

1000 m horizontal offset is of the order of 10^{-12} V/Am^2 (corresponding to about 0.1 of S_{zz} in Figure 14b)—which is again easily detectable using realistically achievable receiver sensitivities, noise levels, and transmitter dipole moments.

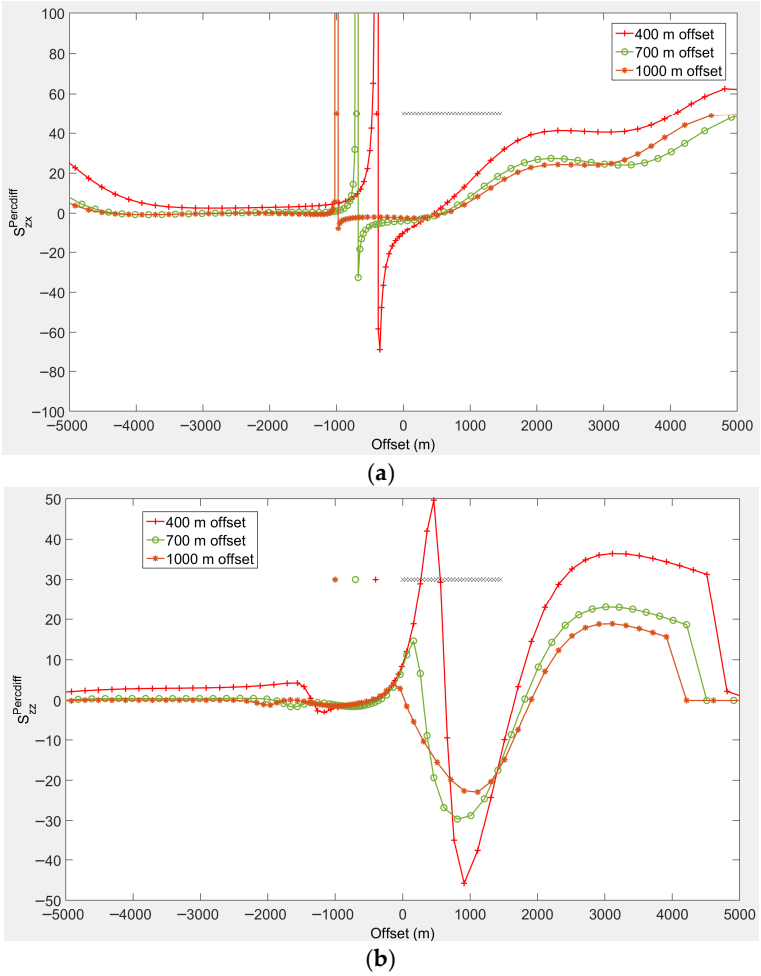


Figure 15. Percentage difference between the modelled response and that of the *half-space reference model* of (**a**) the horizontal and (**b**) the vertical components of the electric field at the seafloor for variants of the *resistive disk model* with a range of horizontal offsets of the borehole from the nearest edge of the target. The locations of the offset source are plotted with corresponding colour markers, and the resistive target is plotted by black 'x' markers.

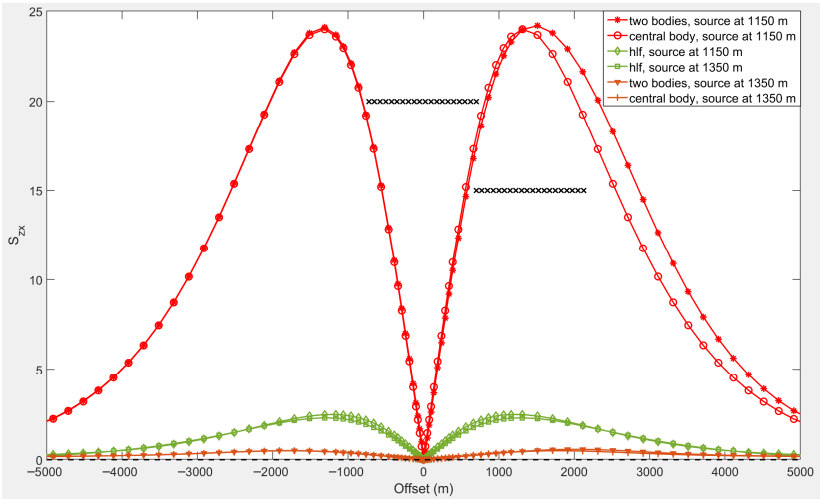
Information about the lateral extent (as opposed to existence and direction) of the resistive target is largely masked in the case of the *just outside* model by the source depth-related field behaviour. However, at the longer (700 m and 1000 m) offsets of the target from the borehole, both the lateral extent and the position of the resistive target become more apparent, but still not exact in the seafloor responses. The responses show that the resistive body has moved but cannot be precisely located.

5.4. Multiple, Stacked Reservoir Targets

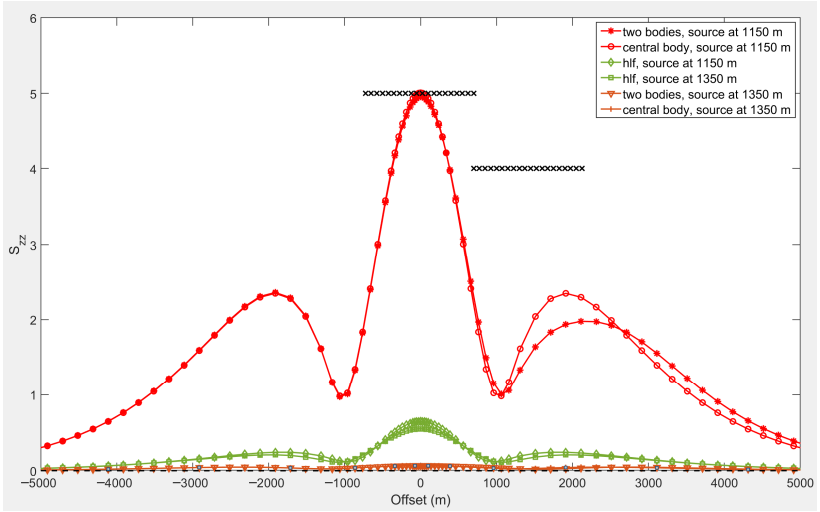
The next part of our study investigates the situation of stacked reservoirs at different depths. For this, we include in our model two resistive bodies, each with dimensions and properties equal to those of the standard resistive disk of the previous model. These are placed laterally so that the borehole containing the transmitter passes through the centre of the first body, while the second body has its nearest edge displaced by 700 m from the borehole (so that its centre is displaced laterally by just under 1400 m). The two resistive disks are placed vertically so that their centres are at 1150 m and 1350 m depths below the

seafloor respectively. Modelling is performed for two VED source depths: 1150 m (within the central, first, shallower body) and 1350 m (below the first body, at the depth of the second body).

The two-body models show responses (Figure 16) which are broadly similar to the single-*centred resistive disk* model response for the corresponding source depth. The equivalent noise level is shown by a dashed line. We have therefore plotted percentage differences in the two-body model responses with respect to the single-*centred resistive disk* model in Figure 17. These results show that the additional, deeper, offset target is detectable, even in the presence of the central target. However, the sensitivity to the deeper target is larger when the transmitter is at the shallower of the two depths and inside the central body than when it is deeper and outside of any resistive body. The responses are detectable and distinguished, especially when the percentage difference is calculated with respect to the central body response (Figure 17). The location of the offset body can be seen in the percentage difference plot of S_{zz} (Figure 17b) more clearly; however, it is difficult to estimate its exact extent.

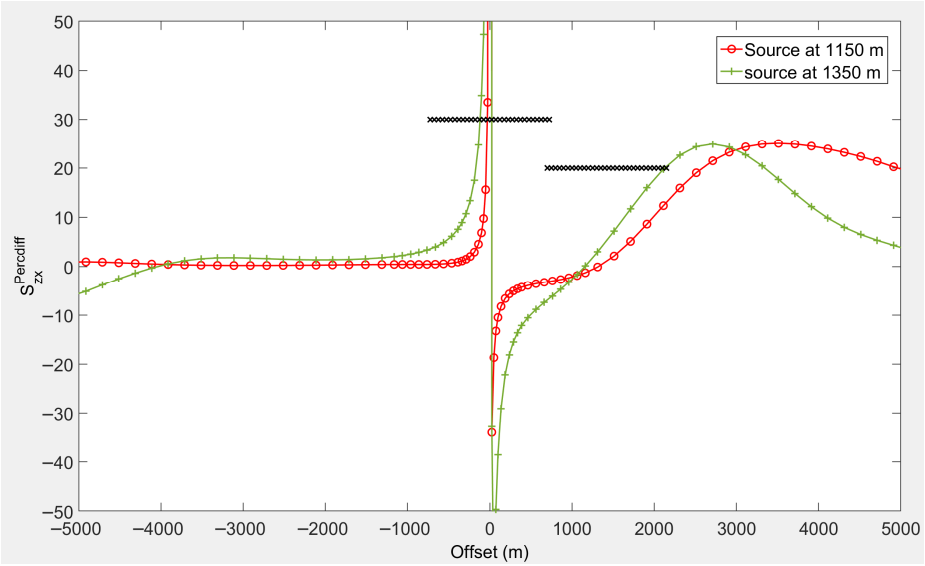


(**a**)

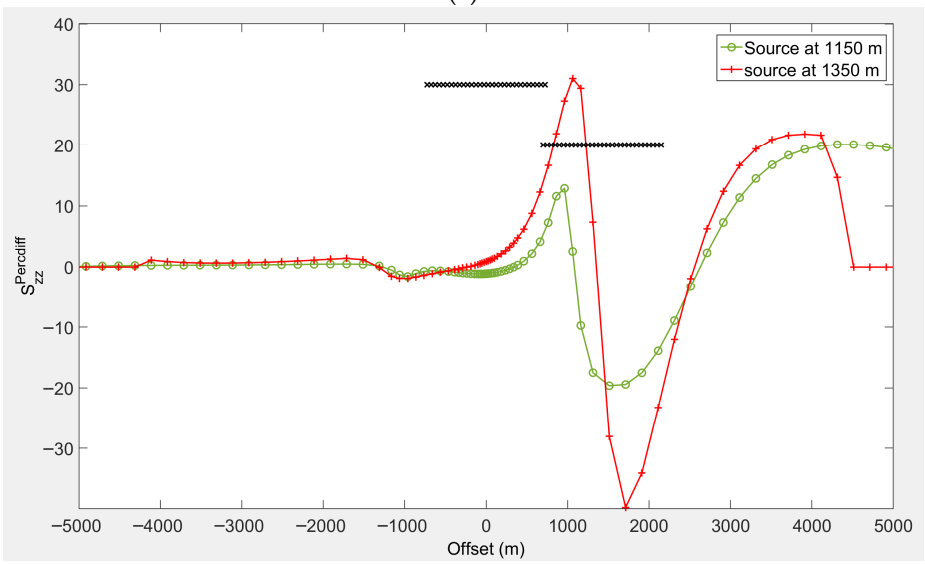


(**b**)

Figure 16. Dimensionless amplitudes of (**a**) the horizontal and (**b**) the vertical components of the electric field at the seafloor for the *stacked reservoir model* for various combinations of resistive targets and transmitter depths. Resistive targets are plotted by black 'x' markers.



(**a**)



(**b**)

Figure 17. Percentage differences in dimensionless amplitudes between the modelled response and that of the corresponding *centred resistive disk model* of (**a**) the horizontal and (**b**) the vertical components of the electric field at the seafloor for the *stacked reservoir model* for two transmitter depths. Resistive targets are plotted by black 'x' markers.

5.5. Deeper Targets

Conventional seafloor to seafloor CSEM surveys progressively lose sensitivity to resistive targets as target depth increases; sensitivity also moves out to longer source receiver offsets. Consequently, detecting resistive targets of realistic and finite lateral extent, around 3 km depth below the seafloor, presents a serious challenge. To investigate the additional value of sbCSEM in such circumstances, we extended our borehole-seafloor modelling to include deeper targets. We repeated the entire model runs, including multiple and offset targets, for target depths of 3 km beneath the seafloor. They show a similar pattern as with the source at 1.1 km depth but with lower amplitude and are therefore not presented here. We only present responses for offset and stacked targets at 3 km depth in Figures 18–20.

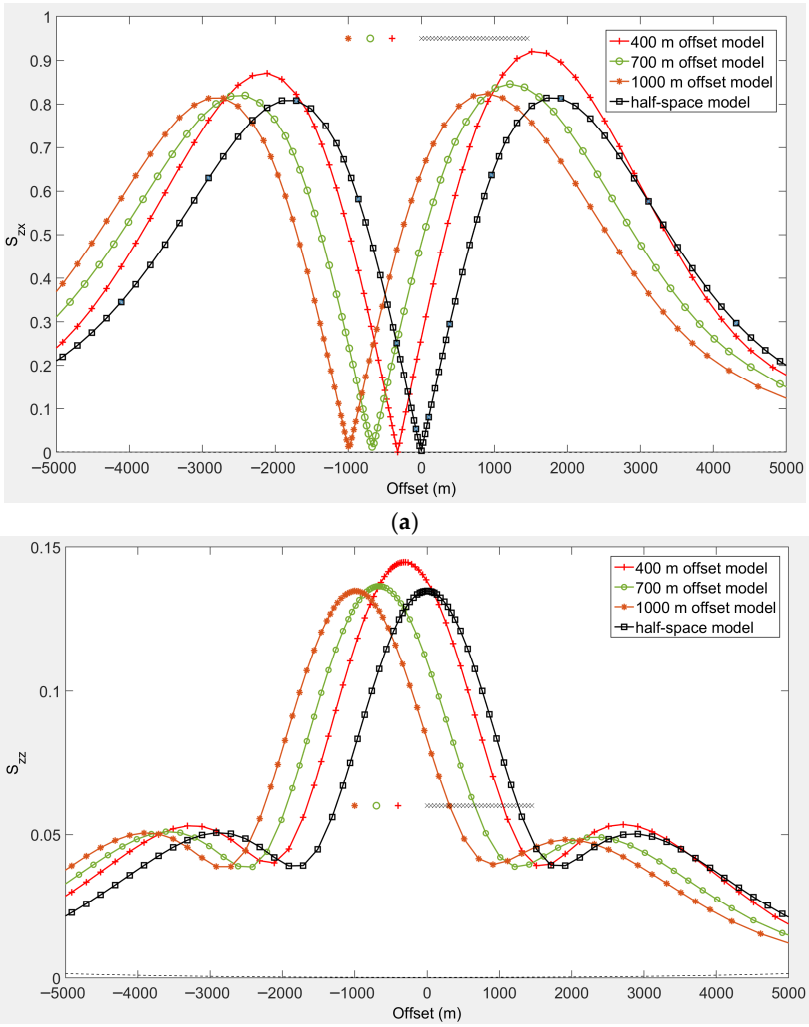


Figure 18. Dimensionless amplitudes of (**a**) the horizontal and (**b**) the vertical components of the electric field at the seafloor for variants of the *resistive disk model* for a range of horizontal offsets of the target and for a target depth of 3 km. The locations of the offset source are plotted with corresponding colour markers, and the resistive target is plotted by black 'x' markers.

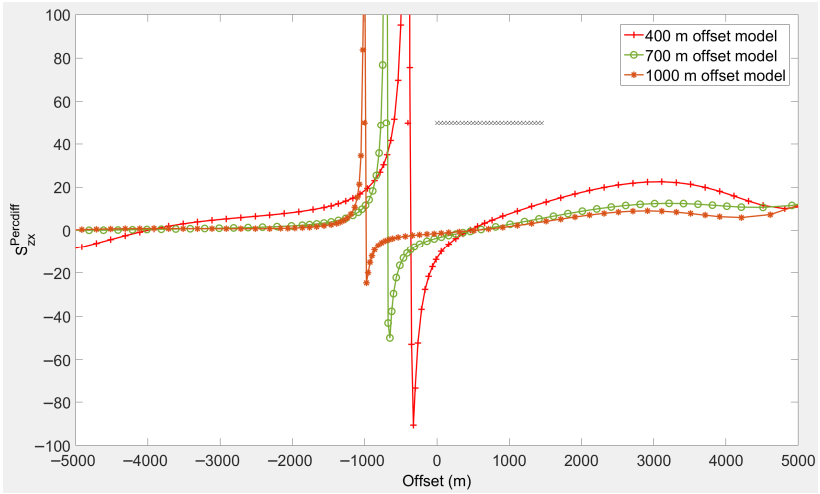
5.5.1. Deeper Single Offset Target at 3 km Depth

As discussed earlier, a much more useful application for the deeper targets is the situation where a well has been drilled to the target depth but has failed to penetrate the resistive body due to lateral mispositioning. To investigate this scenario for the deepest target, the modelling has been repeated for the same offset models as previously, but at 3 km depth. The standard resistive disk target is placed at 400 m, 700 m and 1000 m offset locations. Dimensionless amplitudes and percentage differences with the half-space model of the horizontal and vertical components are shown in Figures 18 and 19, respectively. The results are very similar to those from the offset models at 1.1 km depth. The magnitude of response is less now, but still in the detectable range. For example, a value of around 0.025 for S_{zz} at a 4 km receiver offset location corresponds to the amplitude of E_{zz} in the order of 10^{-13} V/Am^2.

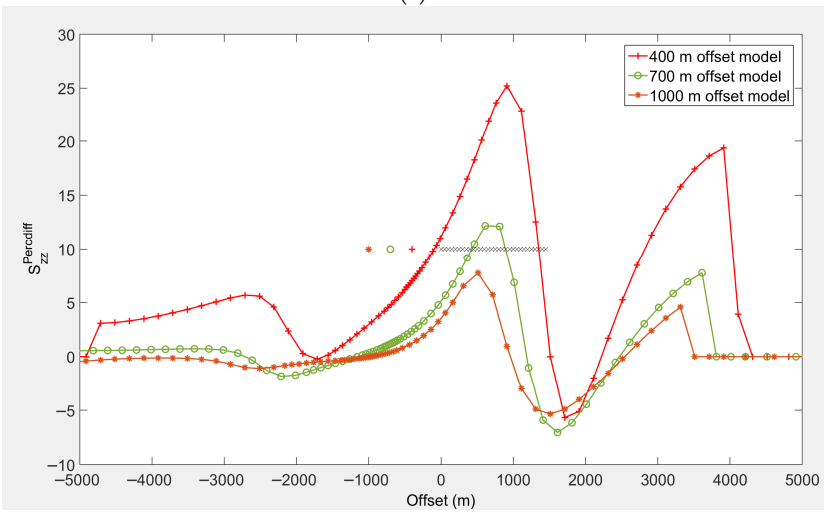
5.5.2. Deeper, Stacked Reservoir Targets

Two-body models similar to those at shallower depths (1.1 and 1.3 km) have been modelled for target and VED transmitter depths of 3 and 3.2 km below the seafloor. The results for percentage difference plots referenced to the corresponding *centred resistive*

disk model are plotted in Figure 20. These responses are somewhat similar to those from 1.1 and 1.3 km depths, although the amplitudes are smaller. The amplitudes should still be detectable, assuming a noise threshold corresponding to 10^{-14} V/Am^2.



(**a**)

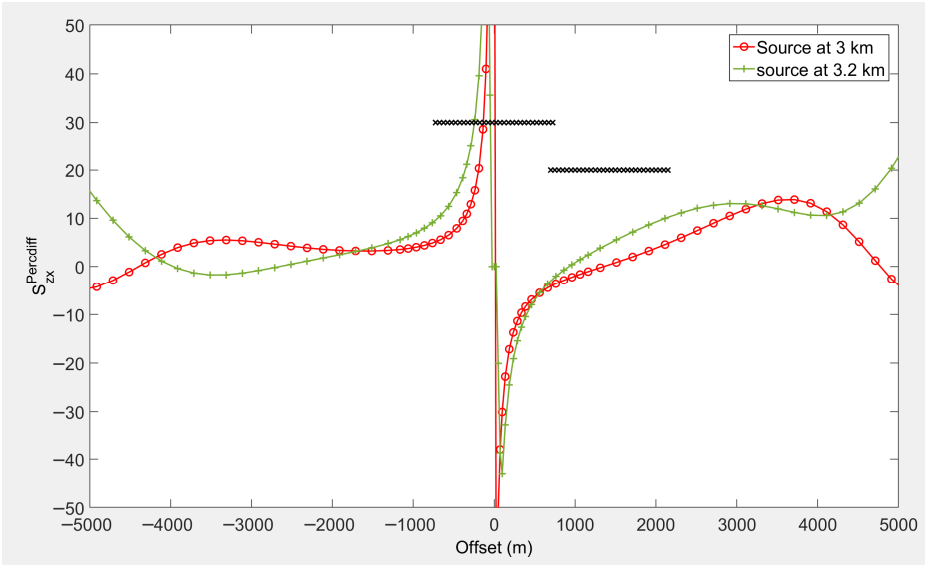


(**b**)

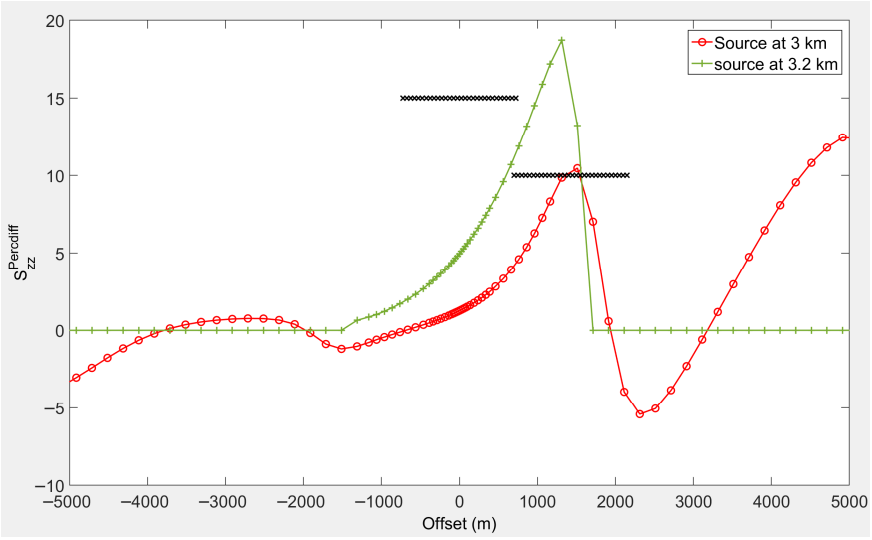
Figure 19. Percentage differences between the modelled response and that of the *half-space reference model* of (**a**) the horizontal and (**b**) the vertical components of the electric field at the seafloor for variants of the *resistive disk model* for a range of horizontal offsets of the target and for a target depth of 3 km. The locations of the offset source are plotted with corresponding colour markers, and the resistive target is plotted by black 'x' markers.

5.6. Vertical Electromagnetic Profiling: VEMP

Our last series of models simulates a different, but potentially exciting, application of sbCSEM: vertical electromagnetic profiling (VEMP), which is a CSEM analogue of vertical seismic profiling (VSP). The results show that a small resistive target can be detected at least 300–400 m before the borehole (or more exactly, a transmitter at the bottom of the borehole) reaches it. Applications of this technique might include looking ahead of the bit before entering the reservoir, or improving estimates of the lateral extent of a reservoir, possibly influencing well sidetrack decisions. This series of model runs is also relevant to scenarios (e.g., CO_2 sequestration projects) in which it is undesirable for the well to pierce the seal above a reservoir, but in which the maximum resolution in terms of total quantity and lateral distribution of the resistive material is required for audit, monitoring or verification purposes.



(**a**)



(**b**)

Figure 20. Percentage differences between the modelled response and that of the corresponding *centred resistive disk model* of (**a**) the horizontal and (**b**) the vertical components of the electric field at the seafloor for variants of the *stacked reservoir model* for two transmitter depths, in which the depths of the two target structures are 3.0 and 3.2 km respectively. Resistive targets are plotted by black 'x' markers.

Figure 21 shows percentage difference between the *centred resistive disk model* and that of the *half-space reference model* of horizontal and vertical components of the dimensionless amplitude in the x-z plane through the transmitter, for a 25 m long VED transmitter located within the overburden at 350 m depth below the seafloor [i.e., with the ends of the dipole at (0, 0, −437.5) and (0, 0, −462.5)]. We can clearly observe the position of the VED source at −450 m in these plots, and that it behaves like a radiating point. We see slightly higher amplitudes of S_{zx} just above the depth of the resistive target (Figure 21a). This appears to be a current blocking phenomenon, with the resistive target layer obstructing vertical current flow within and above the target and tending to deviate the current horizontally. This obstructing and channelling behaviour can also be observed in the plot of S_{zz} (Figure 21b).

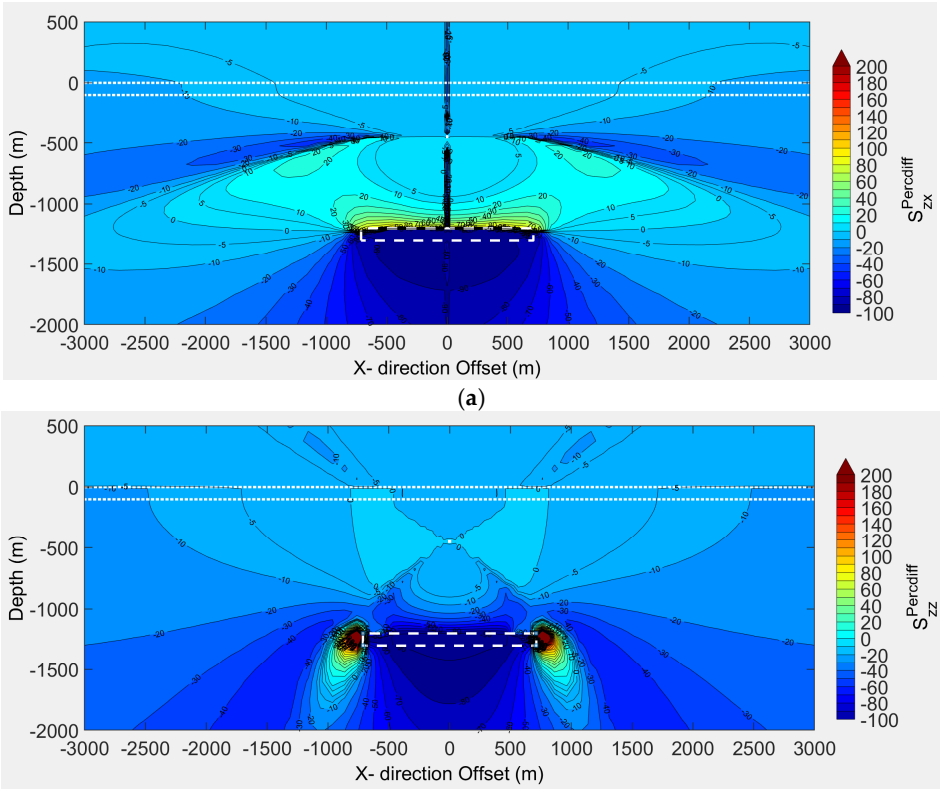


Figure 21. Percentage differences between the *centred resistive disk model* and that of the *half-space reference model* of (**a**) the horizontal and (**b**) the vertical components of the electric field in the xz plane through the transmitter placed at 350 m depth below the seafloor. Water layer is shown by white dotted lines. Locations of the transmitter and resistive disk are marked by a white marker and white dashed lines, respectively.

We have modelled the responses for the *centred resistive disk model* for a series of VED transmitter depths between 50 m and 1450 m below the seafloor. As we move the source up and down within the borehole, the position of the radiating centre moves with it, as expected. The lateral position of the maximum accumulation of S_{zx} at the seafloor also shifts as the depth of the source varies. Other than this, the current blocking and current channelling behaviours associated with the resistive target are broadly similar for all source depths above the target layer. Rather than presenting large numbers of the resulting plots similar to earlier figures, we present a contour plot of the horizontal and vertical components of the responses at the seabed instead.

The percentage difference in the dimensionless amplitude S_{zx} for various source depths ranging from 50 m to 1450 m below the seafloor is shown as a contour plot in Figure 22a. The response is symmetric across the centre of the target; therefore, only the right side of the responses is presented. The horizontal axis corresponds to horizontal source–receiver offset, and the vertical axis corresponds to the transmitter depth. Starting from zero depth and zero horizontal offset (top left), the amplitude initially decreases with increasing source depth. A large increase in amplitudes is observed when the source is within or in contact with the resistive target (~1087 m to ~1212 m depth below the seafloor). The increase in amplitude is maintained as long as at least one pole of the VED source is inside the resistive target. Finally, after the VED source moves completely out of the target, the amplitude suddenly decreases again to its lower value.

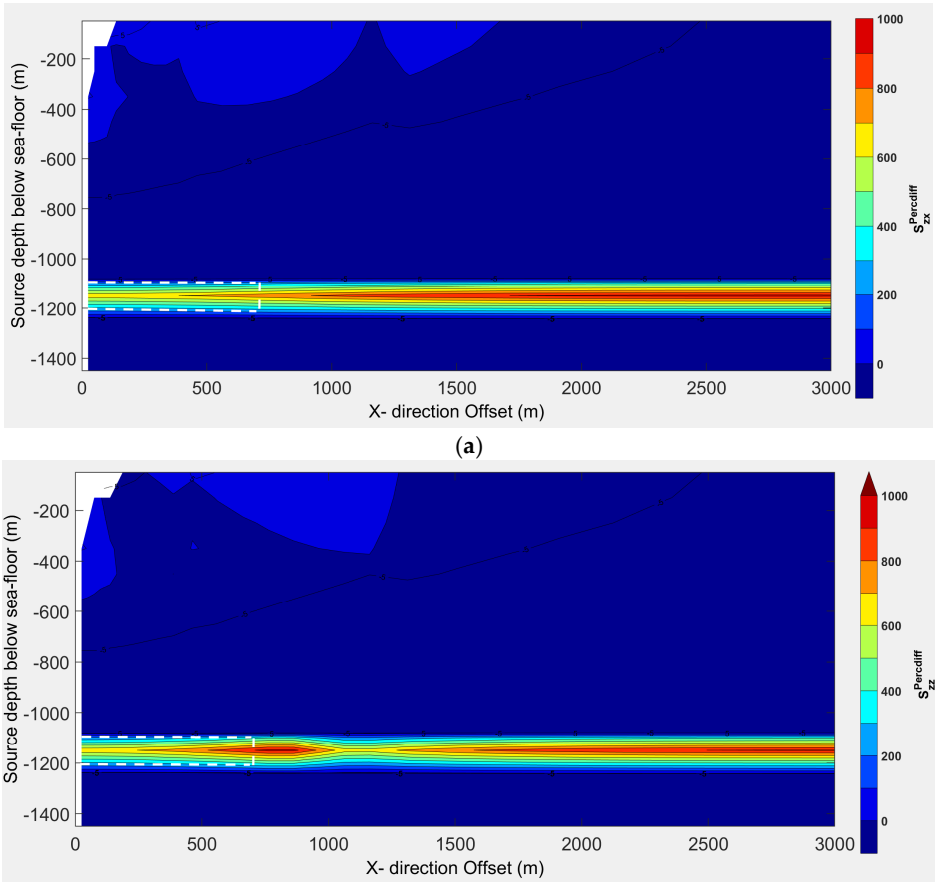


Figure 22. Contour plots of the percentage difference between the *centred resistive disk model* and that of the *half-space reference model* of (**a**) the horizontal and (**b**) the vertical component of the electric field at the seafloor, plotted as a function of the transmitter depth and horizontal transmitter–receiver offset. The location of the resistive disk is marked by white dashed lines.

Figure 22b shows the corresponding percentage difference for S_{zz} responses plotted in the same manner. A large increase in amplitude is again seen when the transmitter is in contact with, or inside, the target body. However, in this case, the lateral extent of this increase in amplitude is limited by the extent of the resistive body itself, with a local minimum along the horizontal direction occurring outside the limits of the resistive body.

We observe that at moderate receiver offsets (around 200 to 700 m), the survey becomes sensitive to the presence of the resistive target at least ~300 m to 400 m before the depth of the target. Interestingly, in this case, the receiver at 1162.5 m offset corresponds to the maximum sensitivity for S_{zx}, but the minimum sensitivity for S_{zz}—an outcome which can be explained by the patterns seen when the transmitter is close to the target depth in Figure 21. This also suggests that the method could be used as down-hole logging by putting a moving source in the borehole and a receiver on the seabed, and vice versa, due to the reciprocity relation.

6. Discussion

Our 3D-modelling results demonstrate that seafloor-to-borehole controlled-source electromagnetic (sbCSEM) configurations exhibit strong sensitivity to the geometry and spatial distribution of resistive targets. In contrast to conventional seafloor-to-seafloor CSEM, the use of a vertical electric dipole (VED) in a borehole introduces a different

coupling mechanism with the subsurface, enhancing sensitivity to resistivity contrasts at depth.

A key observation from the results is the systematic variation in the spatial distribution of the electric field amplitudes at the seafloor. In particular, the occurrence of local minima followed by secondary maxima at offsets approximately related to the transmitter depth reflects the transition between inductive and geometric effects in the electromagnetic response. These features are strongly influenced by the presence of resistive bodies and provide diagnostic information about their position and extent. The lateral displacement of the amplitude maxima in the presence of resistive targets further indicates that sbCSEM responses are sensitive not only to target presence but also to their spatial location.

The results also show that asymmetric resistivity distributions produce corresponding asymmetry in the measured responses. This behaviour is particularly important for scenarios in which the borehole does not intersect the target directly. The ability to detect and characterise laterally offset resistive bodies suggests that sbCSEM may be well suited for step-out exploration, where existing wells are used to investigate surrounding regions for additional hydrocarbon accumulations or other resistive structures.

Detectable variations in the electromagnetic response are observed for targets at depths of up to approximately 3 km, even when the targets have relatively small lateral dimensions (on the order of a few hundred metres). This indicates that sbCSEM configurations can maintain sensitivity under conditions that are challenging for conventional marine CSEM methods, particularly in shallow-water environments where air-wave effects can limit resolution. The results further demonstrate that multiple targets and complex configurations can produce distinguishable signatures, suggesting potential applicability in more realistic geological settings.

The modelling of vertical electromagnetic profiling (VEMP) configurations provides additional insight into the potential of sbCSEM for borehole-based applications. The results indicate that resistive targets can be detected several hundred metres ahead of the borehole, prior to direct intersection. This "look-ahead" capability could be valuable during drilling operations, enabling improved decision-making in real time and reducing exploration risk.

The use of dimensionless amplitudes in the analysis facilitates interpretation by reducing the influence of geometric spreading and emphasising inductive effects. This approach highlights the role of current channelling within conductive layers and current blocking by resistive bodies, which together control the observed response patterns. In addition, the null-coupled tangential electric field component provides enhanced sensitivity to lateral resistivity variations, particularly in non-axisymmetric scenarios, and may offer advantages for delineating target boundaries.

Noise and uncertainty considerations are critical for assessing the practical applicability of the method. In this study, detectability has been evaluated using a nominal noise floor of approximately 10^{-14} V/Am^2 and an assumed survey uncertainty of around 5% in amplitude. These values are broadly consistent with the performance of modern ocean-bottom electromagnetic (OBEM) receivers under favourable conditions. The modelling results indicate that the predicted responses for the scenarios considered remain above these thresholds over a range of offsets, suggesting that detection is feasible in practice.

However, actual survey performance will depend on several additional factors, including receiver sensitivity, instrument stability, positioning accuracy, and environmental noise. Stationary acquisition geometries typically provide more stable and lower-noise measurements, whereas moving-source configurations may introduce additional uncertainties related to navigation and temporal variability. For VEMP-type surveys, precise control of transmitter depth and repeatability of measurements are essential for maintaining data quality.

Despite the encouraging results, there are several limitations. The models considered in this study are intentionally simplified, with homogeneous background resistivity and idealised target geometries. Borehole casing effects, which can significantly influence electromagnetic responses, have not been included. Furthermore, the analysis is based on forward modelling only, and the recoverability of target properties through inversion has not been addressed. These factors may affect the resolution and reliability of the method in real-world applications.

Overall, the results demonstrate that sbCSEM has strong potential as a complementary geophysical technique for exploration, appraisal, and monitoring. Its sensitivity to small, deep, and laterally offset resistive targets, combined with the potential for borehole-based deployment, makes it particularly attractive for challenging environments where conventional methods may be less effective. Further work incorporating realistic geological complexity, casing effects, and inversion-based approaches will be necessary to fully evaluate its practical implementation.

7. Conclusions

This study presents a three-dimensional modelling investigation of seafloor-to-borehole controlled-source electromagnetic (sbCSEM) configurations for the detection of resistive targets in shallow-water environments. The results demonstrate that sbCSEM geometries provide enhanced sensitivity to small, deep, and laterally offset resistive bodies compared to conventional marine CSEM approaches. Source and receiver positions and orientations can be interchanged with each other, based on the principles of reciprocity. Therefore, the method could be applied in practice using either HED or VED sources at or just above the seafloor, and one or more VED receivers placed down the borehole as well.

The modelling shows that resistive targets produce measurable perturbations in both the amplitude and spatial distribution of electric fields at the seafloor. In particular, variations in dimensionless amplitudes and the associated asymmetry of the responses provide diagnostic indicators of target presence, position, and lateral extent. Detectable responses are obtained for targets buried at depths of up to approximately 3 km and for significant lateral offsets from the borehole, indicating the potential of sbCSEM for step-out exploration and reservoir delineation.

The analysis further highlights the role of survey geometry and frequency selection in balancing resolution and signal strength. The use of dimensionless amplitudes enables clearer interpretation of inductive effects by reducing geometric spreading, thereby improving sensitivity to subsurface resistivity contrasts.

The modelling also highlights the potential of vertical electromagnetic profiling (VEMP) for detecting targets ahead of the borehole and for improving estimates of reservoir extent. The null-coupled tangential component offers additional potential for delineating target boundaries. Further work is required to incorporate realistic geological complexity, borehole casing effects, and inversion-based analysis to fully assess practical applicability.

Author Contributions: Conceptualisation, V.C.B., M.C.S. and L.M.M.; methodology, V.C.B., M.C.S. and L.M.M.; software, V.C.B., A.C.M. and Y.S.; formal analysis, V.C.B. and A.C.M.; investigation, V.C.B. and A.C.M.; writing—original draft preparation, V.C.B. and M.C.S.; writing—review and editing, V.C.B., M.C.S. and Y.S.; visualisation, V.C.B.; funding acquisition, M.C.S. All authors have read and agreed to the published version of the manuscript.

Funding: This paper is financially supported by the Technology Programme and the Engineering and Physical Sciences Research Council (UK).

Data Availability Statement: Data associated with this research are available and can be obtained by contacting the corresponding author.

Acknowledgments: We thank the Technology Programme and the Engineering and Physical Sciences Research Council (UK) for providing funding for this research—including salary for VB—under contract no. TP5/OIL/6/H0418J. We also thank Ronnie Parr of BP, Aberdeen, and David Andreis (D.A.) for valuable discussions and advice, and D.A. for the modified 1-D modelling code. We also thank two anonymous reviewers in improving readability and quality of the manuscript in the present form.

Conflicts of Interest: Author Lucy M. MacGregor was employed by the company Rock Solid Images, USA and Edinburgh Geoscience Advisors Ltd., UK. The remaining authors declare that the research was conducted in the absence of any commercial or financial relationships that could be construed as a potential conflict of interest.

References

1. Eidesmo, T.; Ellingsrud, S.; MacGregor, L.M.; Constable, S.; Sinha, M.C.; Johansen, S.; Kong, F.N.; Westerdahl, H. Seabed logging (SBL), a new method for remote and direct identification of hydrocarbon filled layers in deepwater areas. *First Break* **2002**, *20*, 144–152.
2. Ellingsrud, S.; Eidesmo, T.; Johansen, S.; Sinha, M.C.; MacGregor, L.M.; Constable, S. Remote sensing of hydrocarbon layers by seabed logging (SBL): Results from a cruise offshore Angola. *Lead. Edge* **2002**, *21*, 972–982. [CrossRef]
3. Constable, S.; Srnka, L.J. An introduction to marine controlled source electromagnetic methods for hydrocarbon exploration. *Geophysics* **2007**, *72*, WA3–WA12. [CrossRef]
4. Chave, A.D.; Cox, C.S. Controlled electromagnetic sources for measuring electrical conductivity beneath the oceans 1. forward problem and model study. *J. Geophys. Res.* **1982**, *87*, 5327–5338. [CrossRef]
5. Chave, A.D. On the electromagnetic fields produced by marine frequency domain controlled sources. *Geophys. J. Int.* **2009**, *179*, 1429–1457. [CrossRef]
6. Um, E.S.; Alumbaugh, D.L. On the physics of the marine controlled-source electromagnetic method. *Geophysics* **2007**, *72*, WA13–WA26. [CrossRef]
7. Weiss, C.J. The fallacy of the 'shallow-water problem' in marine CSEM exploration. *Geophysics* **2007**, *72*, A93–A97. [CrossRef]
8. Nordskag, J.I.; Amundsen, L. Asymptotic air wave modelling for marine CSEM surveying. *Geophysics* **2007**, *72*, F249–F255. [CrossRef]
9. Andreis, D.; MacGregor, L. Controlled-source electromagnetic sounding in shallow water: Principles and applications. *Geophysics* **2008**, *73*, F21–F32. [CrossRef]
10. Wilt, M.J.; Lee, K.H.; Morrison, H.F.; Becker, A.; Tseng, H.-W.; Torres-Verdin, C.; Alumbaugh, D. Crosshole electromagnetic tomography: A new technology for oil field characterization. *Lead. Edge* **1995**, *14*, 173–177. [CrossRef]
11. Tseng, H.W.; Becker, A.; Wilt, M.J.; Deszcz-Pan, M. A Borehole-to-Surface Electromagnetic Survey. *Geophysics* **1998**, *63*, 1565–1572. [CrossRef]
12. Patzek, T.; Wilt, M.; Hoversten, G.M. Using Crosshole Electromagnetic (EM) for Reservoir Characterization and Waterflood Monitoring. In Proceedings of the SPE Permian Basin Oil and Gas Recovery Conference, Midland, TX, USA, 21–23 March 2000; Extended Abstract; pp. 1–8.
13. Wilt, M.; Morea, M. 3D waterflood monitoring at Lost Hills with crosshole EM. *Lead. Edge* **2004**, *23*, 489–493. [CrossRef]
14. Colombo, D.; McNeice, G.W. Quantifying surface-to-reservoir electromagnetics for waterflood monitoring in a Saudi Arabian carbonate reservoir. *Geophysics* **2013**, *78*, E281–E297. [CrossRef]
15. Scholl, C.; Edwards, R.N. Marine downhole to seafloor dipole-dipole electromagnetic methods and the resolution of resistive targets. *Geophysics* **2007**, *72*, WA39. [CrossRef]
16. Maxey, A.; MacGregor, L.M.; Sinha, M.C. Borehole CSEM for offshore hydrocarbon mapping. In Proceedings of the 8th Workshop on Electromagnetic Induction in the Earth, El Vendrell, Spain, 17–23 September 2006; Extended Abstract.
17. Maxey, A.; MacGregor, L.M.; Sinha, M.C. Borehole CSEM for offshore hydrocarbon mapping. In Proceedings of the 69th EAGE Conference and Exhibition, London, UK, 11–14 June 2007; Extended Abstract.
18. Maxey, A.; MacGregor, L.M.; Sinha, M.C.; Baranwal, V.C. Borehole CSEM for offshore hydrocarbon mapping. In Proceedings of the 4th International Symposium on Three-Dimensional Electromagnetism, Freiberg, Germany, 27–30 September 2007; Extended Abstract.
19. Baranwal, V.C.; Sinha, M.C. Borehole-Seafloor Marine CSEM for Deep and Shallow Water Cases: Some New Insights. In Proceedings of the 19th Workshop on Electromagnetic Induction in the Earth, Beijing, China, 23–29 October 2008; Extended Abstract.
20. Baranwal, V.C.; Sinha, M.C. 3-D Modelling Study of Borehole-seafloor Marine CSEM for Shallow Water Case. In Proceedings of the 71st EAGE Conference and Exhibition, Amsterdam, The Netherlands, 8–11 June 2009; Extended Abstract X022.

21. Cuevas, N.H.; Pezzoli, M. On the effect of the metal casing in surface-borehole electromagnetic methods. *Geophysics* **2018**, *83*, E173–E187. [CrossRef]
22. Pardo, D.; Torres-Verdin, C.; Demkowicz, L.F. Feasibility study for 2D frequency-dependent electromagnetic sensing through casing. *Geophysics* **2007**, *72*, F111–F118. [CrossRef]
23. Kong, F.N.; Roth, F.; Olsen, P.A.; Stalheim, S.O. Casing effects in the sea-to-borehole electromagnetic method. *Geophysics* **2009**, *74*, F77–F87. [CrossRef]
24. Puzyrev, V.; Vilamajo, E.; Queralt, P.; Ledo, J.; Marcuello, A. Three-Dimensional of the Casing Effect in Onshore Controlled-Source Electromagnetic Surveys. *Surv. Geophys.* **2017**, *38*, 527–545. [CrossRef]
25. Yang, W.; Torres-Verdín, C.; Hou, J.; Zhang, Z.I. 1D subsurface electromagnetic fields excited by energized steel casing. *Geophysics* **2009**, *74*, E159–E180. [CrossRef]
26. Yang, Q.; Yue, J.; Tan, M.; Bai, Z.; Wang, W.; Li, B.; Lu, K.; Wang, B.; Zhao, H. 3D Forward Modeling of Borehole-to-Surface Electromagnetic Method with Steel Casing Based on Cylindrical Grid and Analysis of Effective Detection Depth. *Appl. Sci.* **2026**, *16*, 2647. [CrossRef]
27. Hu, Y.; Heagy, L.; Yang, D. Three-dimensional inversion of controlled source electromagnetic data with steel casings. *Geophysics* **2026**, *91*, E13–E26. [CrossRef]
28. Parasnis, D.S. Reciprocity theorems in geoelectric and geoelectromagnetic work. *Geoexplanation* **1988**, *25*, 177–198. [CrossRef]
29. Chen, J.; Oldenburg, D.W.; Haber, E. Reciprocity in electromagnetics: Application to marine magnetometric resistivity. *Phys. Earth Planet. Inter.* **2005**, *150*, 45–61. [CrossRef]
30. Ikelle, L.T.; Amundsen, L. The Concepts of Reciprocity and Green's Functions. In *Introduction to Petroleum Seismology*; Society of Exploration Geophysicists (SEG): Tulsa, OK, USA, 2005; Volume 12, p. 706.
31. Arts, R.; Eiken, O.; Chadwick, A.; Zweigel, P.; van der Meer, L.; Zinszner, B. Monitoring of CO_2 injected at Sleipner using time-lapse seismic data. *Energy* **2004**, *29*, 1383–1392. [CrossRef]
32. Lee, K.H.; Kim, J.H.; Uchida, T. Electromagnetic fields in a steel-cased borehole. *Geophys. Prospect.* **2005**, *53*, 13–21. [CrossRef]
33. Haber, E.; Ascher, U.M.; Aruliah, D.A.; Oldenburg, D.W. Fast simulation of 3D electromagnetic problems using potentials. *J. Comput. Phys.* **2000**, *163*, 150–171. [CrossRef]
34. Sinha, M.C. On the use of dimensionless amplitude units for amplitude data and time units for phase data in marine controlled source electromagnetic studies. In Proceedings of the 18th Workshop on Electromagnetic Induction in the Earth, El Vendrell, Spain, 17–23 September 2006; Extended Abstract.
35. Jiang, F.; Yang, D.; Sun, Z.; Li, F. Inversion of marine magnetotelluric and controlled source electromagnetic data with site gap and low signal-to-noise ratio. *Geophys. J. Int.* **2024**, *238*, 1366–1382. [CrossRef]
36. Maaø, F.A.; Nguyen, A.K. Enhanced subsurface response for marine CSEM surveying. *Geophysics* **2010**, *75*, A7–A10. [CrossRef]

Disclaimer/Publisher's Note: The statements, opinions and data contained in all publications are solely those of the individual author(s) and contributor(s) and not of MDPI and/or the editor(s). MDPI and/or the editor(s) disclaim responsibility for any injury to people or property resulting from any ideas, methods, instructions or products referred to in the content.